Klara Höfler

Suche nach Spuren von nicht-lokalem turbulenten Elektronenwärmetransport in Fusionsplasmen

Technische Universität München
Fakultät für Physik

Abschlussarbeit im Masterstudiengang Applied and Engineering Physics

Suche nach Spuren von nicht-lokalem turbulenten Elektronenwärmetransport in Fusionsplasmen

Search for Signatures of Non-Local Turbulent Electron Heat Transport in Fusion Plasmas

Klara Höfler

25. Januar 2018

Max-Planck-Institut für Plasmaphysik

Erstgutachter (Themensteller): Prof. U. Stroth
Zweitgutachter: Prof. A. Bandarenka

Abstract

Magnetic confinement fusion research has its main application in CO_2 free electricity production. The efficiency of a fusion reactor is directly related to the plasma temperature. The temperature profile is set by heat transport which needs to be in detail understood for feasible power plant construction. Fick's law in general describes heat transport in fusion plasmas which predicts a direct dependence of power fluxes on local plasma quantities, e.g. the local gradient in plasma temperature and plasma density. It has been experimentally confirmed, however, past and current fusion devices have reported experiments where under certain conditions in transient state the local heat flux is no longer a function of the local parameters only.

This thesis presents the search for this kind of violations on the ASDEX Upgrade tokamak and the W7-X stellarator. Transient states in electron heat flux are generated by strong and fast changes of the electron microwave heating, both with sudden on and off power steps after stationary state. The spatially and temporally resolved power flux is obtained by subtracting the radiated and the absorbed power from the heating power and compared to local parameters like the local temperature, its gradient and the density.

A key result is that within the experimental uncertainties no signature of non-local transport is found at the ASDEX Upgrade tokamak. The results point towards a gyro-Bohm-like behaviour. At W7-X non-local effects in transport can neither be excluded nor be confirmed.

Contents

Chapter 1

Introduction

According to estimations of the United Nations the number of the citizens of the world amounts to around 7.5 billion and is daily growing by 230 000 [1]. These people are and will be demanding sufficient energy supply to ensure a fair standard of living. Current electricity generation is highly covered by fossil fuel power plants, facing a rapidly declining availability of their resources and severe environmental issues due to the excessive release of the greenhouse gas CO_2 into the atmosphere which causes the climate on Earth to change drastically [2]. An increasing number of countries is getting aware of this problem, starting to search for CO_2-neutral alternatives, such as fission power plants and renewable energies. It is widely agreed that the first one shall be excluded from considerations of how to design future energy production, as nuclear fission produces radioactive waste which needs final storage for over 200 000 years, accompanied by serious safety concerns. The benefits of renewable energies include decentralised energy generation, independence from dwindling resources and complete CO_2-neutrality [3]. However, the major drawback is the unpredictability of weather phenomena, such as wind strength and hours of sunshine. The solution to overcome power shortages is building large-scale storage systems and/or power plants capable of supplying a base load of power.

One promising, CO_2-neutral and safe candidate is the fusion power plant, which gains energy from fusing light atomic nuclei to heavier ones, the same process taking place at stars. Choosing from various reactants, deuterium and tritium nuclei were found to be the most efficient ones for on earth application in terms of energy exhaust per reaction. In order to enable the fusion of positively charged particles, they need to be given enough energy to overcome the Coulomb-repulsion. A reasonable particle temperature for future fusion power plants is predicted to be in the order of 200

million Kelvin [4] which results in a large heat transport from the hot plasma to the chamber walls of the hosting vessel. On the one hand this heat flux is crucial to further process the energy released by the fusion reactions, on the other hand, it is unfavourable as an oversized energy loss decreases the temperature and therefore needs additional external plasma heating to not terminate the fusion reactions.

Nowadays the two major branches to confine fusion plasmas are magnetic confinement and inertial confinement, whereas this thesis focuses on the former and more developed one. Magnetic confinement means setting up a magnetic field in a specific shape which then traps the charged plasma particles i.e. the components of former neutral atoms: electrons and the remaining positively charged atomic cores, referred to as "ions". Generally the technology to heat, measure and characterise the behaviour of electrons is much more developed than for ions. When considering heat flux, the first step is therefore to investigate electron heat transport and afterwards continue the analysis with ions. Anyway, not only ions but both species need sufficient confinement for achieving fusion, as they permanently experience exchange.

All laboratory plasmas need heating to keep the temperature of the particles high. In the stationary state where constant heating power is supplied, the corresponding heat transport is satisfactorily understood. However, in the transient phase, the very short time after heating power is changed, transport was in some cases found to be different from what is predicted from common diffusion laws. This is what this master thesis is concerned with, to in detail investigate the power balance, heat flux, transport coefficient and heat wave propagation within the first 10–20 ms after an increase or decrease in heating of the electrons.

This thesis is structured as follows: chapter 2 provides information about the theoretical description of heat transport, about plasma confinement, plasma heating methods and experiments claiming the discovery of a violation of diffusive laws. A description of two experimental setups on which experiments were performed and an explanation of diverse plasma diagnostics is given in chapter 3. The results and evaluation of the measured data are discussed in chapters 4 and 6, respectively. Chapter 5 reports on simulations done following experimental results, whereas in the end the main points are summarised and an outlook is given in chapter 7.

Chapter 2

Theoretical Background

2.1 Magnetic Confinement – Tokamak and Stellarator

One of the first questions that arise when talking about plasmas with temperatures around ten times the core temperature of the sun is how to hold them. Plasmas consist of charged particles which due to the Lorentz force follow magnetic field lines, so that their trajectories can be determined by magnetic fields. In magnetic confinement fusion the magnetic field lines are bent to a torus and keep the plasma particles in a "magnetic cage" of toroidal shape. More detailed considerations show that complex field geometries are needed to effectively confine the plasma.

Figure 2.1 depicts the basic properties of a so-called *tokamak* where the toroidal shape of the magnetic field is created by toroidal field coils. Due to plasma drifts, caused for instance by the curved field lines, electric fields or pressure gradients, this configuration alone is not sufficient to fully confine the plasma. For a tokamak an additional poloidal magnetic field, causing the total magnetic field to be helically drilled, is crucial for confinement. This additional field is created by a toroidal plasma current which needs to be externally driven by a transformer having the plasma torus as the secondary winding. As the plasma current can only be induced by a changing flux in the transformer core, and therefore by a changing current in the first winding, the discharges of a tokamak are limited to short times, which is considered to be the major drawback of this configuration. Additional toroidal currents in suitably placed coils can further control the shape of the plasma and the position.

The helically drilled magnetic field of a tokamak is depicted in yellow in figure 2.1 (a). It can be split into the toroidal component (green) which is generated from the toroidal field coils (brown) and the poloidal component (cyan) which is produced by
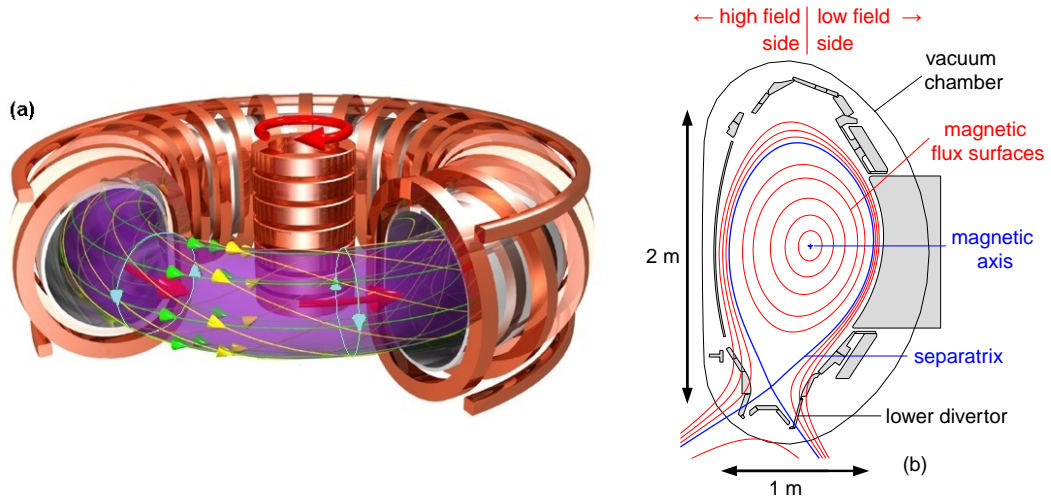
Figure 2.1: The coils (brown) and the helically drilled magnetic field (yellow) of a tokamak (edited from [5]) in (a) and its poloidal cross-section in (b).

the plasma current (red arrows in the purple plasma). The magnetic field strength varies proportional to $1/R$ where R is the *major radius* i.e. the distance to the centre of the tokamak. The geometry of the field lines can be described by the *safety factor* q_s, which is the number of toroidal turns a field line needs to perform one poloidal turn. The geometry consists of areas of constant magnetic flux which are called *magnetic flux surfaces*. They are indicated by the red lines in figure 2.1 (b). Magnetic field lines do not cross these surfaces, instead they lie on them, closing in themselves. The *flux coordinate* ρ is commonly used as spatial dimensionless coordinate, ranging from zero in the *plasma centre* or the *magnetic axis* (blue cross) to one at the *separatrix* (blue line), which separates the magnetic field lines which close inside the torus from those which intersect the vessel wall. The minor radius r measures the same distance in absolute values. The region outside the separatrix, called *scrape-off layer*, directly guides plasma particles and impurities to the *divertor* where they are cooled down and pumped off. Following the strength of the magnetic field, the plasma is divided into the *high field side* which is the inner part of the torus (on the left in figure 2.1 (b)) and the *low field side* which is on the outer part (on the right of (b)), respectively. Depending on the magnetic flux component under

consideration one has to distinguish between ρ_{poloidal} and ρ_{toroidal}. In the context of this thesis the poloidal flux

$$\Psi = \int \mathrm{d}\mathbf{A}_{\text{poloidal}} \cdot \mathbf{B}_{\text{toroidal}}, \tag{2.1}$$

which is the integral of the toroidal magnetic field component over a poloidal area shall be used as spatial coordinate for tokamaks. ρ_{poloidal} is then defined as

$$\rho \equiv \rho_{\text{poloidal}} = \sqrt{\frac{\Psi(\mathbf{r}) - \Psi_{\text{axis}}}{\Psi_{\text{sep}} - \Psi_{\text{axis}}}} \tag{2.2}$$

and for the sake of simplicity abbreviated by ρ in the context of this thesis [6].

Tokamaks are mostly operated in either L-mode (low confinement regime) or H-mode (high confinement regime). The H-mode is characterised by strong turbulence suppression, originating from a so-called *transport barrier* or *pedestal* in plasma temperature and density as well as by high energy confinement times.

In a stellarator both the toroidal as well as the poloidal magnetic field are generated by external coils of complex shape. Figure 2.2 depicts an example of a stellarator configuration, here W7-X. There are three types of coils: planar coils in coppery, non-planar coils in grey and trim coils for fine tuning during plasma operation in yellow. In contrast to tokamaks, the shape of a flux surface depends on the toroidal angle, depicted in figure 2.2 by four representative flux surfaces. Apart from the trim coils, further coils can be used to be more flexible in shaping.

The usual spatial coordinate at stellarators is the normalised effective radius which is equal to ρ_{tor}. The effective radius r_{eff} is defined via the volume

$$V(R, r_{\text{eff}}) = 2\pi^2 R r_{\text{eff}}^2 \tag{2.3}$$

enclosed by a flux surface in a simple torus with poloidal radius r_{eff} and major radius R. $\rho_{\text{tor}}(\mathbf{r})$ is defined as the ratio of $r_{\text{eff}}(\mathbf{r})$ and a_{eff}, which is the effective radius at the separatrix, i.e.

$$\rho_{\text{tor}}(\mathbf{r}) = \frac{r_{\text{eff}}(\mathbf{r})}{a_{\text{eff}}} = \sqrt{\frac{V_{\text{r}}}{2\pi^2 R}} \cdot \sqrt{\frac{2\pi^2 R}{V_{\text{a}}}} = \sqrt{\frac{V_{\text{r}}}{V_{\text{a}}}}. \tag{2.4}$$

Since in stellarator geometry no plasma current is needed for confinement, the ex-
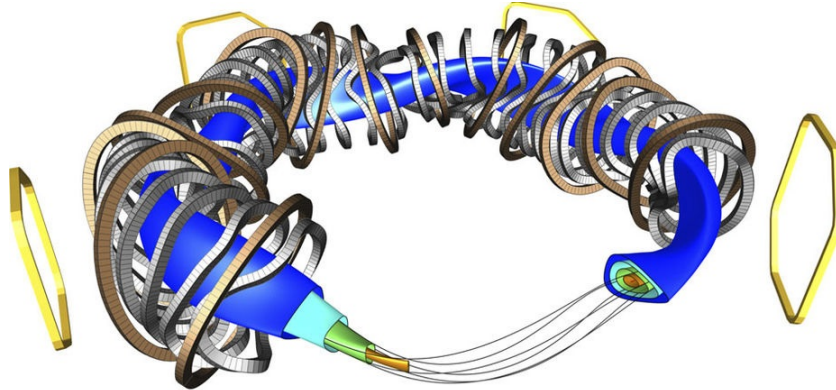
Figure 2.2: Schematic of a stellarator where two different coil systems (coppery and grey) are sufficient to produce a magnetic field for plasma confinement [7].

ternal magnetic field generated by superconducting coils allows plasma discharges of indefinite length. This feature is especially favourable for future energy supply from fusion, making stellarators – regardless of their constructional challenges – promising candidates for fusion power plants.

2.2 Critical Parameters for Fusion

A plasma is said to be ignited when no heating power is supplied but its temperature does not decrease over a "long" time, meaning that the thermonuclear power from the fusion processes balances the power losses. Rephrasing this comparison as a formula gives the *ignition condition* or *Lawson criterion* [6]

$$nT\tau_{\mathrm{E}} \geq 5 \cdot 10^{21} \text{ keV s } /\mathrm{m}^3. \tag{2.5}$$

According to the Lawson criterion, the product of plasma particle density n, temperature T (which in plasma physics is usually in units of eV: 1 eV $= 1.6 \cdot 10^{-19}$ J) and energy confinement time τ_{E} (characteristic time in which the plasma loses its energy) must be larger than a critical value. The plasma in a future power plant does not

necessarily have to fully ignite, the crucial relation is that the energy output is much larger than the energy input. The corresponding figure of merit is

$$Q = \frac{P_{\text{fusion}}}{P_{\text{in}}},\tag{2.6}$$

which for a power plant should be at least 10, raising the basic goal of the ITER tokamak (currently under construction in Cadarache) to reach $Q \geq 10$ as well [4]. n is then aimed to be in the order of 10^{21} m^{-3}, T in the order of tens of keV and τ_{E} about 1 s. For reaching these values the plasma needs large heating as well as reduced heat and particle transport which will be both discussed in the following. Section 2.3 presents different forms of plasma heating and section 2.4 deepens power balance considerations, introduces heat transport and transport models.

2.3 Plasma Heating

The fusion of a deuterium and tritium core releases 17.6 MeV of energy which in a future power plant will be partially extracted as heat and in the following converted to electricity, but also used to heat the plasma and keep fusion processes running. External heating is needed when the plasma is generated starting from a cold torus as well as in power plants without fully ignited plasmas. Various techniques (which can be looked up in literature, like [6]) have been developed to supply power to the plasma, some key methods are described here.

2.3.1 Ohmic Heating

The toroidal current which is responsible for sustaining tokamak-confinement is also a source of plasma heating. Due to the large difference in mass, it is mainly carried by the electrons other than the ions. The name "Ohmic heating" comes from the resistivity of the plasma, caused by collisions between the moving particles. Ohmic heating is always present and important in tokamaks, whereas it is only relevant in a stellarator in case it is actively driven.

2.3.2 Electron Cyclotron Resonance Heating

In the context of this thesis the electron cyclotron resonance heating (ECRH) is of major importance, because it exclusively heats electrons and can moreover drive a plasma current in addition to the already existing plasma current if the microwave beam is obliquely injected.

The general concept is based on resonance: injected electromagnetic waves couple with electrons at certain frequencies and transfer energy. For a better understanding of this mechanism one has to go back to the very simple picture of a charged particle being trapped in a magnetic field. Due to the Lorentz force it gyrates around the field lines with a certain frequency, the gyrofrequency

$$\omega_c = \frac{|q|B}{m}. \tag{2.7}$$

q and m refer to the charge and mass of the particle. B is the magnitude of the local magnetic field strength and can be approximately expressed as $B(\mathbf{r}) \approx B_{tor}(\mathbf{r}) = B_{tor}(R) \propto \frac{1}{R}$ because in a typical tokamak the toroidal field is much stronger than the poloidal field. This unambiguous relation between the magnetic field and the major radius allows an accurate mapping where the heating power is deposited in terms of flux coordinates. Both plasma species, electrons and ions are sensitive to microwave heating. The required frequency for electrons lies in the microwave range at a few hundred GHz, depending on the magnetic field (usually a few Tesla). For ions the corresponding frequency is a few tens of MHz.

The electromagnetic waves for electron microwave heating are produced in a so-called *gyrotron* inside of which an electron beam is shot into a parallel magnetic field with increasing amplitude. Taking advantage of the conservation of the magnetic momentum the high parallel kinetic energy is to a large extend converted into orthogonal energy. The electrons partially get rid of their energy via radiation, which is guided to the plasma and absorbed by the plasma electrons.

2.3.3 Neutral Beam Injection

Another possibility to increase the temperature is injecting high energetic neutral particles with $E_{kin} \gg E_{therm}$ in the plasma which transfer their kinetic energy E_{kin} to the plasma particles via collisions and increase their thermal energy E_{therm}. These

collisions can induce a charge exchange process where a fast neutral particle takes over the charge of a slow plasma ion which is then no longer confined and hits the vessel walls. The other possibility of interaction is ionisation of the neutral particle, either via collisions with ions or electrons. For beams with low particle energies, charge exchange is the dominant effect with the largest cross-section, whereas for high energetic beams the cross-section for ionisation by ions is of major importance. For ionisation by electrons it is low. In order to not raise the impurity density while heating and to have a good scattering cross-section the beam particles should equal one of the main plasma species.

2.4 Heat Transport

This section introduces basic equations which state that heat transport at one point in space depends on local plasma quantities only. However, it has been observed in experiments and some theories and simulations show, that different plasma regions can couple over larger distances in a time scale faster than heat diffusion. In other words the heat flux at one spatial location then also depends on the evolution of plasma parameters at another location.

2.4.1 Energy Balance

Heat transport is in general driven by spatial gradients in temperature. In magnetically confined plasmas another important parameter is the direction of transport relative to the magnetic field lines. Transport is much faster in parallel direction, i.e. along magnetic field lines than perpendicular to them. Owing to this the plasma temperature and density are to a good approximation constant along a flux surface. Energy loss in fusion reactors is carried by *radial transport* perpendicular to the magnetic field and perpendicular to the magnetic flux surfaces. This is the component which is looked at in plasma transport studies.
A general description of the evolution of temperature and heat flux is given by the energy equation for thermal plasmas. It is obtained by considering the plasma as a many-particle system, taking the velocity distribution function and deriving with respect to time, which leads to the Boltzmann equation. Integration of the Boltzmann equation multiplied by the second moment of velocity over the whole

velocity space gives the link between the microscopic many particle system and macroscopic physical quantities which can be measured in experiment. Some terms of the energy equation can then be neglected for thermal plasmas as considered in the context of this thesis. Finally sources and sinks are introduced which results in the energy balance equation

$$p_{\text{in}} - p_{\text{out}} = \frac{\partial}{\partial t}\left(\frac{3}{2}Tn\right) + \nabla \cdot \left(\mathbf{q} + \frac{5}{2}T\mathbf{\Gamma}_{\text{n}}\right), \tag{2.8}$$

for which a detailed derivation is given in [8]. All quantities in equation 2.8 can depend on radius and time. p_{in} and p_{out} are sources and sinks of power density. The product of the plasma temperature T and its density n equals the kinetic pressure p and is a measure for the energy in the plasma. The heat flux per time in units of power per area is $\mathbf{q}$ and the number of particles flowing over a certain surface per time is $\mathbf{\Gamma}_{\text{n}}$. Applying some maths and rearranging equation 2.8 will show that power input and output are balanced by a change in plasma energy and particle and heat transport, respectively. First, it is integrated over the volume inside a flux surface. This is trivial for the source and sink terms on the left hand side of equation 2.8 which become the total power input and output inside the flux surface. The other terms shall be discussed in more detail.

Internal Plasma Energy

After the integration the first term on the right hand side of equation 2.8,

$$\int \frac{\partial}{\partial t}\left(\frac{3}{2}Tn\right)\mathrm{d}V = \frac{\partial}{\partial t}\int \frac{3}{2}Tn\,\mathrm{d}V = \frac{\partial}{\partial t}W, \tag{2.9}$$

corresponds to the temporal derivative of the plasma energy inside ρ

$$W(\rho) = \int\limits_{0}^{V(\rho)} \frac{3}{2}\left(n_{\text{e}}T_{\text{e}} + n_{\text{i}}T_{\text{i}} + n_{\text{imp}}T_{\text{imp}}\right)\mathrm{d}V. \tag{2.10}$$

W is the volume integral over the plasma temperature, weighted by the plasma density times the factor 3/2 which refers to the degrees of freedom. T_{e} and n_{e} are the temperature and density of the electrons, respectively, T_{i} and n_{i} of the main

ion species (mostly hydrogen or deuterium), and T_{imp} and n_{imp} of the (positively charged) impurities, mostly coming from the vessel wall.

Heat Conduction and Convection

Applying Gauss's law the second and third term on the right hand side of equation 2.8 can be rewritten as a two-dimensional integral over a flux surface;

$$\int \nabla \cdot \left(\mathbf{q} + \frac{5}{2} T \mathbf{\Gamma}_{\mathrm{n}} \right) \mathrm{d}V = \int \left(\mathbf{q} + \frac{5}{2} T \mathbf{\Gamma}_{\mathrm{n}} \right) \cdot \mathrm{d}\mathbf{A} = \int \mathbf{q} \cdot \mathrm{d}\mathbf{A} + \frac{5}{2} \int T \mathbf{\Gamma}_{\mathrm{n}} \cdot \mathrm{d}\mathbf{A}. \quad (2.11)$$

For radial transport as discussed before, all vector quantities can be replaced by their scalar magnitude, because heat and particle flux are parallel to the normal vector of the magnetic flux surface. The heat flux term becomes

$$\int \mathbf{q} \mathrm{d}\mathbf{A} = \int q \cdot \mathrm{d}A = Q, \quad (2.12)$$

with Q as the total power flowing over a magnetic flux surface. In the convective part T can be taken out of the integral because its value is constant on a magnetic flux surface. The particle flux is then given as

$$\frac{5}{2} \int T \mathbf{\Gamma}_{\mathrm{n}} \cdot \mathrm{d}\mathbf{A} = \frac{5}{2} T \int \Gamma_{\mathrm{n}} \, \mathrm{d}A = \frac{5}{2} T \Gamma_{\mathrm{N}} \quad (2.13)$$

with $T\Gamma_{\mathrm{N}}$ as the total power being transported over a magnetic flux surface by convection. Experiments and calculations based on complex gyrokinetic equations have shown that in the *plasma core* ($\rho < 0.9$), heat transport is highly dominated by diffusive transport [9]. As this thesis focuses on the mentioned region, the convective part of equation 2.11 will be neglected in the following.

Coming back to spatial gradients which cause heat and particle flux, Fick's law for the power flux is

$$q(\rho) = -\chi(\rho) n(\rho) \nabla T(\rho) = \frac{Q(\rho)}{S(\rho)}, \quad (2.14)$$

which gives a direct dependence of q on the local gradient of the temperature. χ is referred to as the transport coefficient or diffusion coefficient which is determined
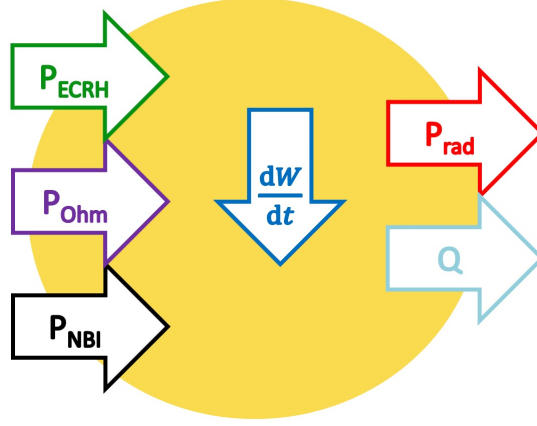
Figure 2.3: Power balance in the plasma (yellow): plasma heating as power source (left), absorbed energy by the plasma (middle) and power losses as radiation and heat flux (right).

by transport models and has the physical units m^2/s. $S(\rho)$ is the area of the flux surface.

2.4.2 The Power Balance Equation

All terms remaining from the previous section plugged together result in the so-called *power balance equation*, valid for plasmas in the context of this thesis:

$$P_{\text{heat}} = P_{\text{ECRH}} + P_{\text{Ohm}} + P_{\text{NBI}} \approx \frac{\mathrm{d}W}{\mathrm{d}t} + Q + P_{\text{rad}}. \tag{2.15}$$

The heating power has to be either absorbed by the plasma ($\frac{\mathrm{d}W}{\mathrm{d}t}$), transported to colder plasma regions as heat flux (Q) or radiated away as bremsstrahlung or from line emissions (P_{rad}). Note that the left hand side of equation 2.15 does not exactly equal the right hand side, as heat transport due to convection is neglected. Figure 2.3 gives the schematic of the power balance for the sum of all plasma particles. As equation 2.15 not only holds for the whole plasma but is also valid for the power within a flux surface, the yellow region either represents the whole plasma or the plasma within a flux surface. It directly refers to the principle of energy conservation. Although at least two species (electrons and ions) are present in a plasma, one can

consider the power balance of one species only. In this case additional source or sink terms

$$P_{\mathrm{e,i}} \propto n_{\mathrm{e}} n_{\mathrm{i}} \frac{T_{\mathrm{e}} - T_{\mathrm{i}}}{T_{\mathrm{e}}^{3/2}}, \quad P_{\mathrm{i,e}} \propto n_{\mathrm{e}} n_{\mathrm{i}} \frac{T_{\mathrm{i}} - T_{\mathrm{e}}}{T_{\mathrm{e}}^{3/2}} \tag{2.16}$$

are required in equation 2.15, which contain the energy transfer between the species [10]. The latter increases for larger temperature differences between the species and can be kept small for low plasma densities. The power balance equation for electrons only is

$$P_{\mathrm{e,heat}} = P_{\mathrm{ECRH}} + P_{\mathrm{e,Ohm}} + P_{\mathrm{e,NBI}} \approx \frac{\mathrm{d}W_{\mathrm{e}}}{\mathrm{d}t} + Q_{\mathrm{e}} + P_{\mathrm{e,rad}} + P_{\mathrm{e,i}}, \tag{2.17}$$

with the internal electron energy

$$W_{\mathrm{e}}(\rho) = \int\limits_{0}^{V(\rho)} \frac{3}{2} n_{\mathrm{e}} T_{\mathrm{e}} \, \mathrm{d}V. \tag{2.18}$$

2.4.3 The Transport Coefficient

For known plasma densities, temperatures and radiated power, the proportionality constant of Fick's law (equation 2.14), the transport coefficient

$$\chi(\rho) = -\frac{1}{n(\rho)\nabla T(\rho)S(\rho)} \cdot \left(P_{\mathrm{heat}}(\rho) - \frac{\mathrm{d}W}{\mathrm{d}t}(\rho) - P_{\mathrm{rad}}(\rho) \right) \tag{2.19}$$

can be calculated for each magnetic flux surface $S(\rho)$. P_{heat}, $\dot{W}_{\mathrm{e}}$ and P_{rad} correspond to the power deposited, absorbed and emitted, respectively, in the volume enclosed by the flux surface. As transport models are included via χ, a detailed examination of this quantity and its dependencies is of major interest.

Initial theoretical transport studies suggested diffusive transport caused by collisions between the plasma particles. In this case the transport coefficient is the product of a characteristic length which the particles travel between collisions and the square of the collision frequency: $\chi = l_{\mathrm{c}}\nu^2$. Reasonable values for l_{c} are in the order of the *Larmor radius* (the radius of the circular trajectory of a charged particle gyrating around a magnetic field line). In more advanced models it is of the order of the radial size of the so-called *Banana orbit*. Trapped plasma particles, i.e. particles where the

ratio between the velocity component parallel and perpendicular to the magnetic field is smaller than a certain value, cannot follow a magnetic field line several times around the torus. Instead they are reflected at locations where the magnetic field strength exceeds a critical value and bounce back and forth. Due to the plasma drifts stemming from the inhomogeneous and curved magnetic field, the way back does not take place at the same field line as the way forth. The name of the trajectory comes from its projection on a poloidal plane which looks like a banana. This mechanism opens a short-cut between different flux surfaces which are separated by the width of the banana orbit and strongly increases transport between them.

The transport coefficient derived from these two models highly underestimates experimentally observed flux values. Therefore it is believed that a large fraction of heat flux is driven by turbulence which can be modelled by gyro-kinetic theory. In particular, the existence of a critical temperature gradient threshold is indicated, above which transport is large, whereas it is small beneath it. Different models for χ have been developed. A simple model for good experimental examination is the *critical gradient model*.

2.4.4 The Critical Gradient Model

According to the critical gradient model, turbulence and thus electron heat transport strongly increase above a threshold in $|R\nabla T_e/T_e| = |R/L_{T_e}|$, called κ_c and referred to as the *critical (temperature) gradient*. R is the major radius of the torus. For $|R\nabla T_e/T_e| < \kappa_c$ electron transport is assumed to be low, the electron transport coefficient χ_e is proportional to a small χ_0, produced by background turbulence. Above this threshold, χ_e strongly depends on the local temperature and the local temperature gradient. It is also a function of the local safety factor q_s, the flux surface averaged magnetic field strength B and a coefficient χ_s. These relations are summarised in

$$\chi_e = \chi_0 T_e^{3/2} q_s^{3/2} \frac{\sqrt{m_i}}{e^2 B^2 R} + H\left(-\frac{R\nabla T_e}{T_e} - \kappa_c\right) \cdot \chi_s T_e^{3/2} q_s^{3/2} \frac{\sqrt{m_i}}{e^2 B^2 R}\left(-\frac{R\nabla T_e}{T_e} - \kappa_c\right),$$
(2.20)

where H is the Heaviside function, e is the elementary charge and m_i the mass of a plasma ion [11]. The parameters χ_0, χ_s and κ_c are radially dependent, but can

approximately be assumed to be constant. More details about the spatial dependence of κ_c can be for instance found in [12] and [13].

In the experiments described in chapter 4, the temperature and its gradient strongly depend on time (due to changing plasma heating power), whereas the time dependence of the remaining parameters listed in equation 2.20 can be neglected. Fick's law (c.f. equation 2.14) using the electron transport coefficient from the critical gradient model becomes

$$q_{\mathrm{e}}(\rho) = -\chi_{\mathrm{e}}(\rho)n_{\mathrm{e}}(\rho)\nabla T_{\mathrm{e}}(\rho) = -\tilde{\chi}_{\mathrm{e}}T_{\mathrm{e}}^{3/2}(\rho)q_{\mathrm{s}}^{3/2}(\rho)n_{\mathrm{e}}(\rho)\nabla T_{\mathrm{e}}(\rho), \qquad (2.21)$$

where the electron temperature and the safety factor are pulled out of the transport coefficient. The exponent of T_{e}, $3/2$, represents the so-called *gyro-Bohm scaling*, which stands for diffusive transport with a scale length proportional to the ion Larmor radius. According to the critical gradient model the power flux is not a function of temperature gradient and density only, but also depends on other plasma parameters such as the electron temperature and the safety factor, which are, however, all local.

2.5 Simulating Heat Transport

In order to recognise non-local transport as such, one needs to focus on the transient state. This is because for any stationary profile, a radially dependent diffusion coefficient can describe the transport processes within the experimental error bars [14]. This section focuses on the basic understanding of simulations performed with the transport code ASTRA (Automated System for TRansport Analysis) in order to deepen the theoretical understanding of electron heat transport in transient state.

2.5.1 Automated System of Transport Analysis

The ASTRA code is a transport code for predictive and interpretative transport modelling, for stability analyses and for processing experimental data. The user can implement arbitrary transport models and in the process of the simulation tune them until a reasonable agreement between experimental data and modelling results is achieved.

For given boundary and initial conditions ASTRA solves four basic transport equations, one for each, the electron density, the electron temperature, the ion tem-
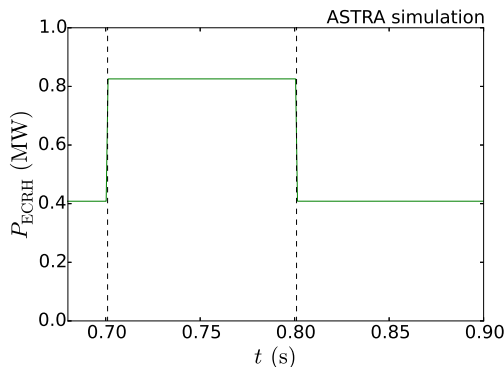
Figure 2.4: Sudden change in ECRH power used for ASTRA simulations.

perature and the currents in the plasma. Building on the results of this, ASTRA then calculates the plasma equilibrium, i.e. the magnetic field configuration and can reconstruct experimental measurements [15].

2.5.2 Simulations of Local Transport

For a basic understanding of transport this section simulates local transport. As only heat transport of electrons shall be studied in this thesis, it is advantageous to purely change the electron heating and decouple ions from electrons. The best candidate for this purpose is electron cyclotron heating. Consider the case of having a plasma in stationary state where suddenly microwave heating is switched on and later switched off again (see figure 2.4).

The simulated reaction of the electron temperature is shown in figure 2.5 (a) for adding and in (b) for removing ECRH power. For the sake of simplicity the transport coefficient is assumed to be a parabolic function in ρ and constant in time. The dashed black line on the left side is the temperature profile in stationary state. Starting from this profile in (a), some ECRH power ΔP_{ECRH} is added at $\rho = 0.18$. The ECRH deposition region is a Gaussian function of the flux coordinate (black dotted line in figure 2.5). Four representative temperature profiles in the transient state are chosen and plotted in different colours. Directly after the change in heating the profile changes most, especially close to the ECRH deposition radius. The blue and green lines are electron temperature profiles 1 and 4 ms after the ECRH power step. As time evolves, the temperature approaches a new stationary state, where
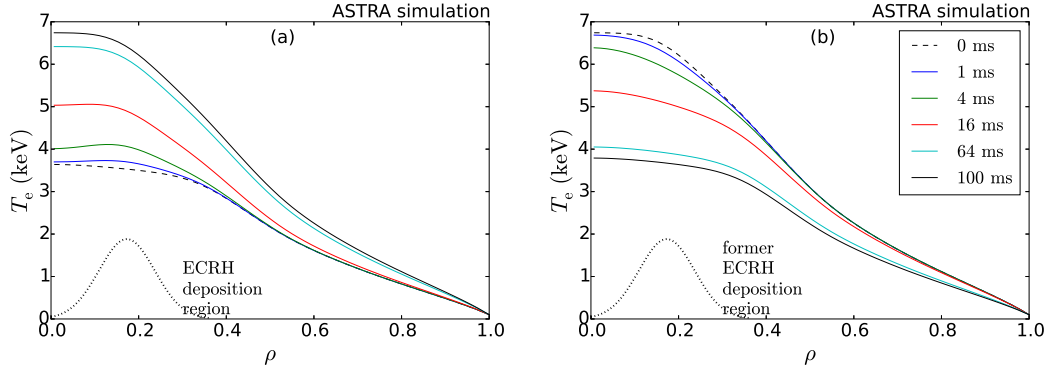
Figure 2.5: Electron temperature profile evolution for switching on (a) and off (b) central electron cyclotron resonance heating.

the time derivative of the stored plasma energy is again zero, but the gradients of the profiles are different from what they have been before when ECR heating was switched off. The entire discussion also holds for the reversed process: switching ECR heating off in the centre, depicted in figure 2.5 (b).

In order to track the propagation of the heat wave through the plasma, a crucial point for further considerations is the finite response of T_e at different ρ. When the heating power is increased in the centre, it results in an increase of temperature which spreads outwards, starting from the place of heating. Within the first few milliseconds the plasma edge has not yet received the information about heating. For the sake of simplicity the boundary condition of the temperature is assumed to be independent of time (i.e. $T_e(\rho = 1) = \text{const.}$).

The temperature evolution shown in figure 2.6 (a) points out the same behaviour: the time it takes the plasma edge temperature (purple line) to be given the information of heating in the core of the plasma, is around $\Delta t_{0,\text{sep}} = t_{\text{heat}} - t_{0,\text{sep}} \approx 10$ ms for this simulation and a few ms for experiments which will be shown later (the purple line is flat in this scaling, however, the red line indicates the same behaviour for 2 ms).

The energy of the electrons enclosed by a magnetic flux surface at ρ, $W_e(\rho)$, in figure 2.6 (b), rises as the electron temperature. As long as the heat pulse has not yet reached the separatrix (the separatrix temperature gradient has not increased after switching on ECRH and by that has not enabled larger heat flux), all heating power
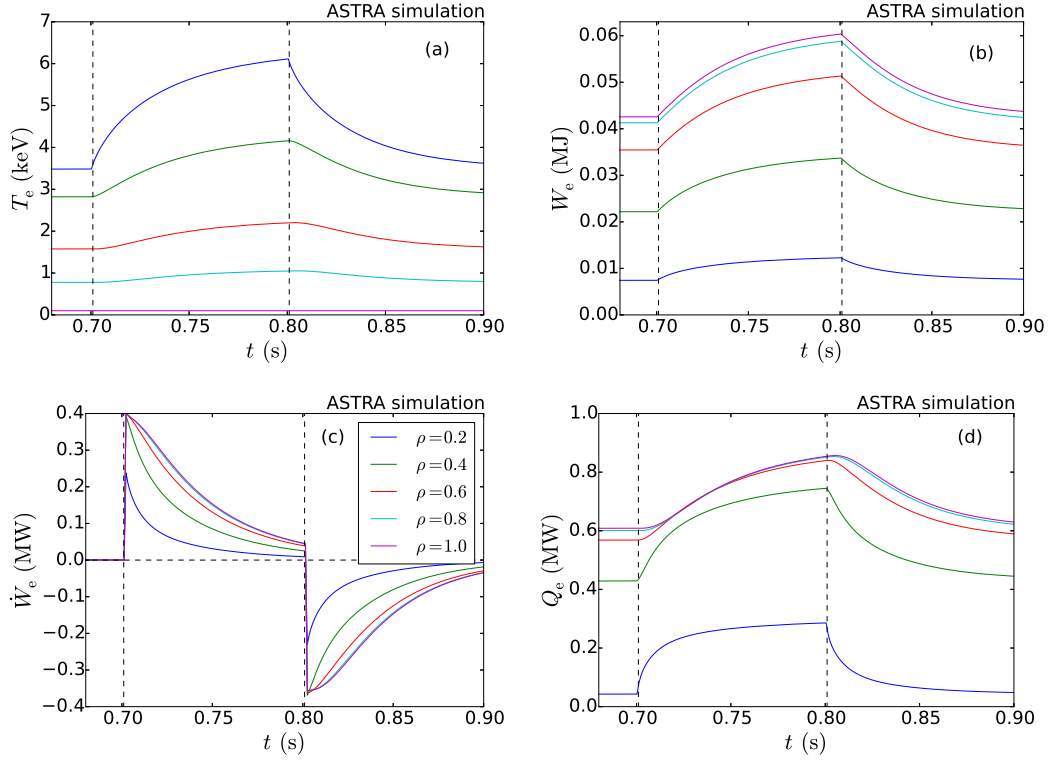
Figure 2.6: Response of electron temperature (a), electron energy (b) and its derivative (c) and the power flowing over one flux surface (d) on sudden changes in ECRH power, simulated with ASTRA.

is absorbed by the plasma. This statement well summarises the simplified picture of the power balance equation and predicts a linear rise of the kinetic energy from t_{heat} until $t_{0,\text{sep}}$. In this simulation, however, it is not fulfilled, as this formulation neglects radiative power losses and power exchange to the ions. Though, infinitesimally after t_{heat}, it holds true, shown by the time derivative of the electron energy, which exactly compensates P_{ECRH} for flux surfaces outside the heating deposition region, shown in figure 2.6 (c). The power flowing over the separatrix remains constant during $\Delta t_{0,\text{sep}}$ (purple line in figure 2.6 (d)) and then changes smoothly, whereas the power flow further in shows the same behaviour, but reacts earlier on heating.
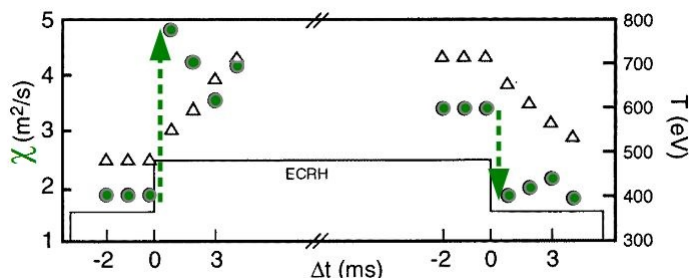
Figure 2.7: At W7-AS the transport coefficient at a spatial area reacts like a step function to a step in heating power deposited at a different spatial location [16].

2.6 Experiments Pointing to Non-Local Transport

In this section, non-locality shall be explained by experiments, which report that χ does not depend on local quantities only. In other words they claim to see transport as non-local phenomenon because the power balance in transient states is not fulfilled experimentally. All missing power is assumed to be part of heat flux as this cannot be directly accessed via experimental diagnostics.

2.6.1 Step in the Electron Transport Coefficient

At the W7-AS stellarator transport studies based on ECRH switching on and off indicated a direct dependence of the transport coefficient on the heating power [16]. The continuous black line in figure 2.7 depicts ECR heating power which is suddenly increased, causing the electron temperature (triangles) averaged over $0.35 < \rho < 0.85$ to rise and saturate at a specific value. It is argued that the temporal change in internal plasma energy is not high enough to come up for the change in heating power. A non-negligible fraction of P_{heat}, the so-called *missing power* cannot be tracked and is assumed to be transported away as heat Q. This raises the necessity for Q to jump when P_{ECRH} jumps. As the temperature gradient stays unchanged, Fick's law is violated. The transport coefficient (averaged over $0.35 < \rho < 0.85$) changes stepwise even though all local quantities have not changed yet, which can only explained if χ does not depend on local quantities only. Missing power was also reported by [17].
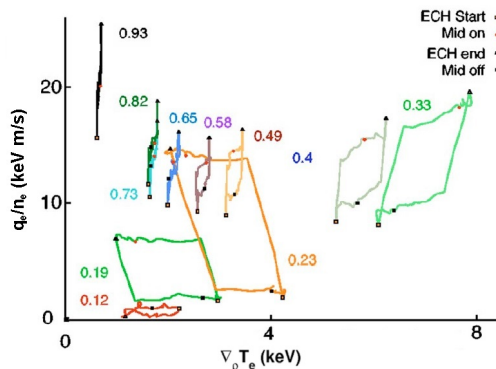
Figure 2.8: Hysteresis in electron power flux per density over the electron temperature gradient. Measured at DIII-D [18].

2.6.2 Ambiguous Electron Heat Flux over Electron Temperature Gradient

At the DIII-D tokamak ECRH modulation experiments have been performed with a modulation frequency of 25 Hz [18]. 0.7 MW of ECRH power was deposited at $\rho = 0.2$ into a discharge of 0.6 MW of continuous ECRH power at $\rho = 0.3$. The electron power flux q_e over the density shows hysteresis behaviour when plotted over the electron temperature gradient, see figure 2.8. [18], [19] and [20] interpret this hysteresis to directly point to non-local transport, as they see a violation of Fick's law according to which they claim that for one electron temperature gradient there cannot be two different values of the heat flux.

Note that in this argumentation any time dependence of the electron transport coefficient is neglected, which will be in more detail discussed in section 4.4.2 and section 5.2.

Chapter 3

Experimental Setup

This work comprises results from two different toroidal fusion experiments: the ASDEX Upgrade tokamak and the W7-X stellarator. In the following both experiments and some of their measurement diagnostics shall be introduced and characterised.

3.1 The ASDEX Upgrade Tokamak

ASDEX Upgrade (Axial Symmetric Divertor EXperiment) is operated in Garching bei München since 1991. It uses pure deuterium, hydrogen or helium as working gas, so fusion processes are kept negligible. The most relevant technical parameters of commonly conducted experiments and their maximal values in brackets are listed in the following table [21].

Parameter	Value
major plasma radius	1.65 m
minor plasma radius	0.5 m
magnetic field	2.5 T (3.4 T)
plasma current	1 MA (1.2 MA)
pulse length	10 s
plasma volume	13 m^3

The following sections give an overview of the diagnostics measuring plasma parameters which are used for transport and power balance studies at ASDEX Upgrade

(AUG). The physical quantities together with the diagnostics which are used to measure them in the context of this thesis are written in the subsequent table.

measured quantity	short form	diagnostic
electron temperature	T_e	electron cyclotron emission (ECE) or integrated data analysis (IDA) based on ECE and Thomson scattering spectroscopy (TS)
electron density	n_e	IDA based on TS, lithium beam emission spectroscopy and infra-red laser interferometry
ion temperature	T_i	charge exchange recombination spectroscopy on NBI
ion density	n_i	$\approx n_\mathrm{e}$
radiated power	P_rad	bolometer

3.1.1 Electron Cyclotron Emission

As explained in section 2.3.2, electrons in a magnetic field emit electromagnetic radiation with angular frequencies $\omega = n\omega_\mathrm{ce}$, where ω_ce is the electron cyclotron frequency and n the harmonic number. This process is the same which takes place inside the resonator of a gyrotron. Inside a narrow region where ω_ce, T_e and n_e are approximately constant the wave is repeatedly absorbed and re-emitted (in case of having a so-called *optically thick plasma* which is usually fulfilled). The electromagnetic waves leaving this place to the antenna are not any more absorbed by plasma. The electromagnetic spectrum coming from a certain area equals black body radiation with the intensity

$$I(\omega) = \frac{\omega^2 T_\mathrm{e}(R)}{8\pi^3 c^2} \tag{3.1}$$

as a function of the wave frequency ω. Similarly to ECR heating the B-dependence of ω_ce is used to obtain spatial resolution for temperature profile reconstruction [6]. The emission is mainly in so-called *X-mode*, where the electric field of the wave

oscillates perpendicular to the background magnetic field. At ASDEX Upgrade the intensities are measured with a heterodyne radiometer consisting of 60 channels with 1 cm radial resolution [22].

3.1.2 Thomson Scattering

This diagnostic is based on the injection of a high intensity laser into the plasma. The plasma particles which are intersected by the laser beam start oscillating at the wave frequency which corresponds to the laser wave length. They then radiate at a slightly different frequency, which is Doppler shifted due to the thermal motion of the particles. The Doppler broadening of this light relates to T_e, whereas its intensity is a measure for n_e [23].

3.1.3 Lithium Beam Emission Spectroscopy

The Li-BES diagnostic injects a beam of neutral lithium particles into the plasma and measures the interaction between the beam and the plasma particles. Collisions between them either ionise the lithium particles or excite their electrons into higher atomic states. The state which is occupied most is 2p. Via de-excitation and emission of a photon it then relaxes back to 2s. Using the probabilistic lithium beam data analysis, the plasma density is extracted from the spatial distribution of these photons. This diagnostic is particularly suited for edge density measurements and yields a high spatial and temporal resolution [24].

3.1.4 Infra-red Laser Interferometry

The *plasma frequency* ω_p directly relates to the characteristic time in which the plasma reacts to changes in electric fields. Electromagnetic waves of frequencies ω_w below ω_p cannot pass the plasma, whereas for $\omega_w \gg \omega_p$ the behaviour is like in vacuum. If ω_w is in the same order of magnitude (but strictly larger) as ω_p the phase velocity is decreased when the wave passes through the plasma. In comparison to a beam travelling the same distance in pure vacuum, the beam going through the plasma experiences a phase shift which is proportional to the plasma density integrated along the path [6].

3.1.5 Integrated Data Analysis

At ASDEX Upgrade the integrated data analysis uses the Bayesian probability theory to combine the measurements of different diagnostics to provide the most probable electron temperature and density profiles. T_e is obtained from ECE and TS whereas n_e stems from Li-BES, deuterium cyanide laser interferometry and TS [25].

3.1.6 Bolometer

In a bolometer the radiated power coming from the plasma heats a thin film (e.g. a thin metal resistance thermometer, a semiconductor or a pyroelectric detector). After an absolute calibration, the measured rate of change in temperature can be referred to the radiated power [6]. This includes not only radiation stemming from the confined plasma, but also large contributions from the divertor region and the scrape off-layer.

3.1.7 Charge Exchange Recombination Spectroscopy

As stated in section 2.3.3 the fast particles of the neutral beam heating deposit their kinetic energy amongst others via charge exchange. The original plasma ion is left in an excited state with one more electron than before. In case of deuterium it is neutral, in case of an impurity ion with higher mass number it might stay positively charged. The excited state decays through photon emission at characteristic frequencies, [26]. From the Doppler broadening of these spectral lines the bulk thermal temperature of the emitting ions can be determined, [27].

3.2 The W7-X Stellarator

The W7-X (Wendelstein 7-X) stellarator is operated in Greifswald since 2015. It is the largest experimental fusion facility of its type and was built to experimentally proof the suitability of stellarators to perform as fusion power plant. The arrangement of its magnetic field is shown in figure 2.2. It is generated by 50 superconducting coils and is commissioned to enable plasma discharges of up to 30 minutes. As in ASDEX Upgrade the working gas is either hydrogen or helium (deuterium after ≈ 2020). The main device parameters are listed in the following table, [28].

Parameter	Value
major plasma radius	5.5 m
minor plasma radius	0.53 m
magnetic field	2.5 T (3.0 T)
pulse length (commissioned but not yet performed)	30 min
plasma volume	30 m^3

The diagnostics available to measure the plasma parameters necessary for studies on electron heat transport at W7-X do not differ from those used at ASDEX Upgrade and will not be again explained.

Chapter 4

Experimental Results from ASDEX Upgrade

This chapter presents experiments performed on the ASDEX Upgrade tokamak. The basic interpretation of the electron temperature evolution comes first and is followed by calculations of the heat flux and detailed discussions about signs for the existence or non-existence of non-locality in electron heat transport on AUG.

4.1 Experiment Design

For investigations of non-local transport five plasma discharges were carried out at ASDEX Upgrade. Given that non-locality can only be detected in transient states, the switching on and off of ECRH power is crucial. Typical AUG plasmas need a couple of hundred milliseconds to reach stationary state after a change in heating. The time between switching-processes in the experiments is for instance 250 ms to enable good equilibration of the plasma, but also 17 ms which allows perturbative analyses (ECRH modulated with a frequency of 29.4 Hz). Adding and removing one gyrotron to ECRH power takes less than a millisecond (i.e. happens "suddenly").
The changes in heating occur on top of background ECRH power for three reasons: first, this counteracts large changes in Ohmic heating power during ECRH switching processes. Second, it facilitates corresponding simulations with the transport code ASTRA. Third, for suppression of a periodically occurring (period $\approx$ 15 ms) plasma instability called the *sawtooth instability*, one gyrotron additionally to electron microwave heating drives a current (ECCD – electron cyclotron current drive). By that the safety factor is modified in a way that it does not fall below the value 1, which

would, in case of unfavourable shear (which relates to the safety factor and its spatial derivative) trigger this instability. In order to not generate relativistic particles by putting too much power per particle, the base load gyrotron is set to heat away from the plasma centre ($\rho \approx 0.32$), whereas the gyrotrons for the power steps heat closer ($\rho \approx 0.25$).

In general studies on turbulent transport prefer L-mode plasmas which do not suffer from so-called *edge localised modes* typical for H-mode-plasmas. In order to stay in L-mode the first shot scenario was designed to be "upper single null" where the open magnetic field lines ($\rho > 1$) hit the upper divertor and the power threshold for reaching H-mode becomes higher. Due to a poor conditioning of the upper divertor this configuration accumulated a large tungsten concentration in the plasma which strongly increased radiation losses. The remaining shots therefore used lower single null and gained much better radiation values.

Two plasma scenarios are used in the context of this thesis: scenario I with power steps at low frequency and scenario II with ECRH modulation at different radii.

4.1.1 I – Power Steps

Figure 4.1 shows the time traces of some plasma parameters of shot #34927 performed in scenario I design. For sawtooth suppression the plasma current I_P (a) is chosen to be low. The three power sources (ECRH, Ohmic and NBI) and one power sink, the radiated power measured by the bolometers, are depicted in figure 4.1 (b). The difference in ECRH power is the same for the whole shot. This on the one hand allows averaging the data over several power steps and on the other hand gives information about the reproducibility and the evolution of the plasma parameters over a large time window. One gyrotron drives a current at $\rho = 0.32$, whereas another gyrotron is switched on and off at $\rho = 0.26$, first with a period of 500 ms, then 200 ms. At $t = 4.59$ s it failed, so only two instead of nine planned short power steps were actually done. In the end a third gyrotron deposits power at $\rho = 0.16$. The Ohmic power reacts to the ECRH steps in a way to keep the plasma current constant. When switching on, the temperature and therefore the plasma conductivity increase. In order to keep the plasma current constant, the Ohmic power has to decrease. The black lines are NBI blips which provide short time windows for ion
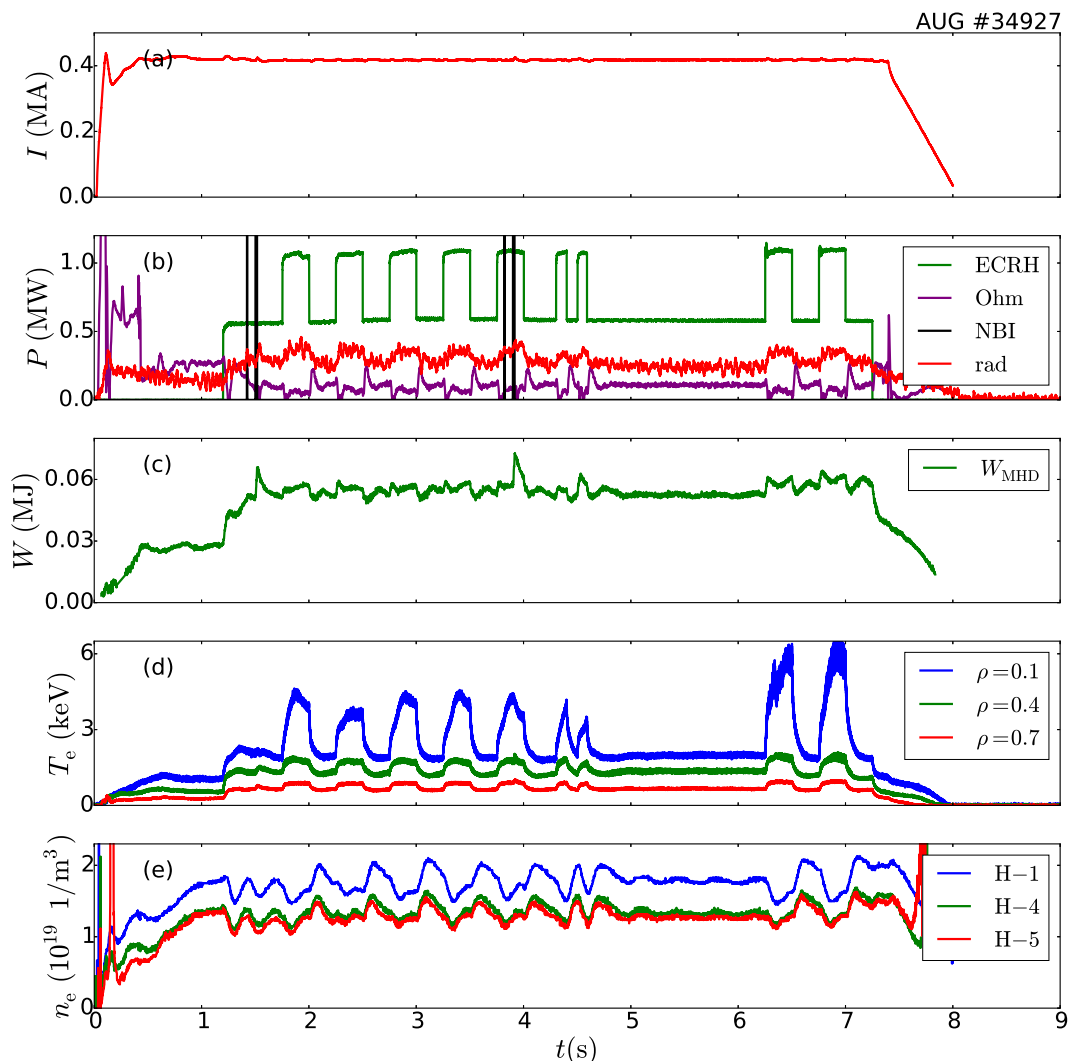
Figure 4.1: Time traces of the plasma current (a), the heating power and radiated power (b), the plasma energy (c), the electron temperature from ECE (d) and the electron density from interferometry (e) for a scenario I discharge.

temperature measurements at dedicated time points. The radiated power is coloured in red and also reacts on the ECRH steps, c.f. section 4.3.2.

The impacts of changes in heating can clearly be seen in the plasma energy W_{MHD}, calculated from pick-up coil measurements (c), as well as in the electron temperature T_e from ECE which is given for three radii (d). Figure 4.1 (e) depicts the electron

density taken from three interferometer measurements with different lines of sight through the plasma (referred to as H-1, H-4 and H-5). The choice of a low n_e for this discharge has two effects: first, it prevents the plasma from reaching H-mode, and second, it permits pure electron transport studies, because ions and electrons are only weakly coupled at low densities. In order to study only transient behaviour in temperature rather than in density, n_e was held as constant as possible via gas puff feedback.

4.1.2 II – Fast Modulation in Power

Scenario II is a reproduction of scenario I except for the ECRH power. Its magnitude is modulated with a period of 34 ms, i.e. the time between two consecutive processes of switching on. As depicted in figure 4.2 (a), ECRH modulation takes place in three different time windows, each lasting for 1.7 s, which only differ by the radial deposition of the heating power ($\rho = 0.58, 0.70, 0.79$). One gyrotron with current drive constantly deposits at $\rho = 0.31$. The density shown in figure 4.2 (b) is controlled via a fixed gas puff rate (feed forward). The electron temperature (c) changes only little because the modulation period is larger than the characteristic time T_e needs to rise. Figure 4.2 (d) depicts a zoom into the electron temperature data measured by ECE. The response to heating changes is similar for each switching process, a stationary state is not reached. Hence, the background gradients do not undergo significant modifications which validates perturbative analysis methods for this scenario.

4.2 Electron Temperature: Transport Time, Spatial Gradient

In this section, the spreading of the injected power and the heat flux after switching on and off ECRH power is investigated. As response to a sudden change in heating power, the temperature rises, starting from the radial position of maximum power deposition. According to Fick's law the change in heat flux cannot propagate on a time scale much faster than the change in local temperature gradient. However, in non-local transport it is observed to do so. This section provides a detailed analysis of the electron temperature which will be subsequently used for transport
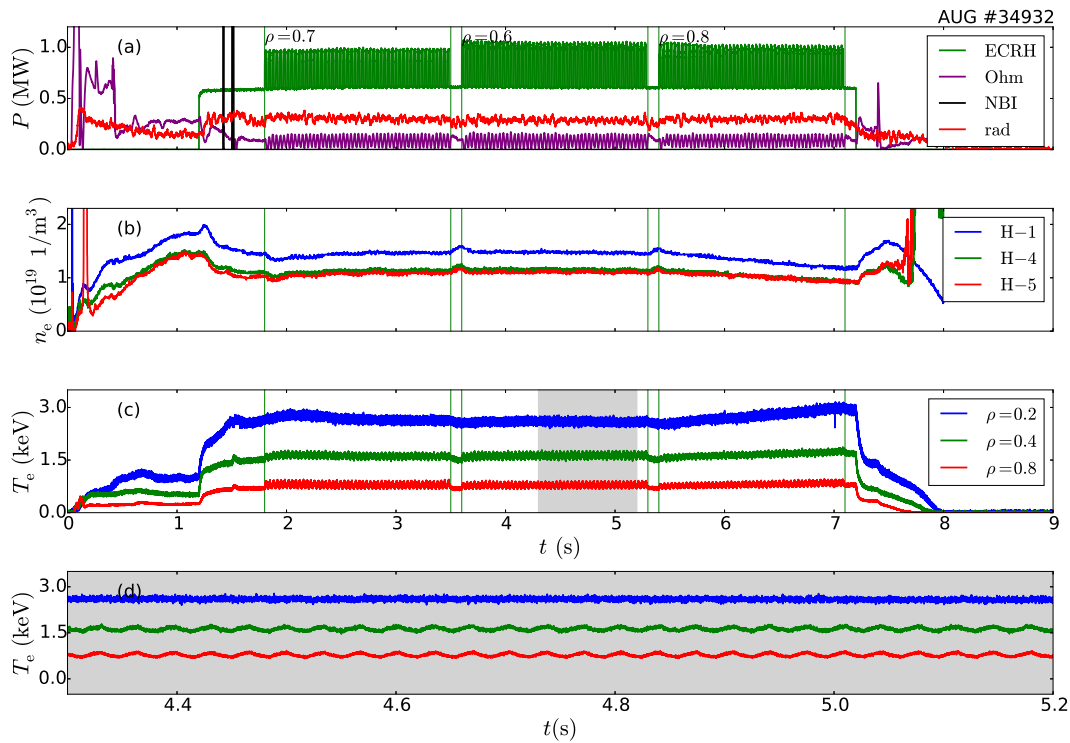
Figure 4.2: Time traces of the heating power and radiated power (a), the electron density from interferometry (b) and the electron temperature from ECE (c),(d) for a scenario II discharge.

interpretations in terms of Fick's law, for calculations of the kinetic plasma energy and the estimation of time constants which describe the propagation of heat pulses.

4.2.1 Profile Evolution after Change in Heating

The evolution of the electron temperature profile measured by ECE (circles) and IDA (full line) during a transient state in shot #34927 is shown in figure 4.3. ECRH power is added (dotted curve in (a)) and removed (same in (b)) in order to generate the transient state. The system starts in stationary state, represented by the dashed black line in (a). Then heating is added and the temperature profile changes. Different colors correspond to temperature profiles at different times after ECRH switching on. After 230 ms another stationary state is reached (full black line). The same description holds for the reversed process (b) where heating is switched off and
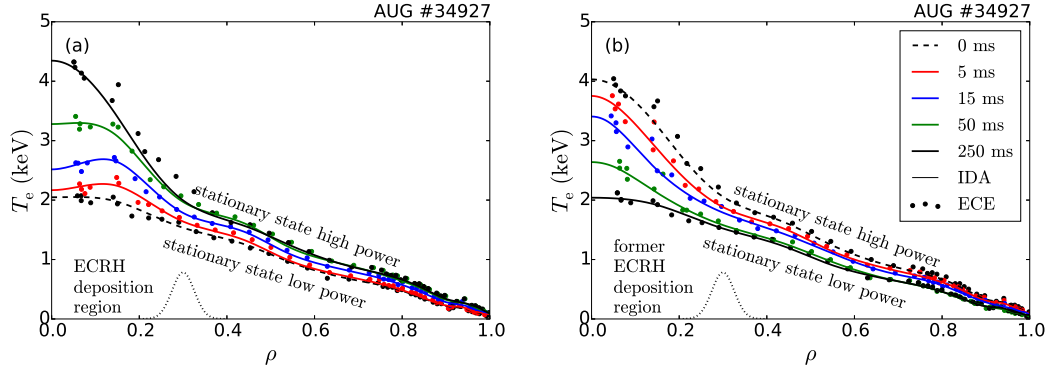
Figure 4.3: T_e profile evolution for adding off-axis ECRH (dotted line) at $t = 2.25$ s (a) and removing it at $t = 2.50$ s (b).

the plasma evolves from the stationary state at high heating power to the stationary state at low power.

As ECR heating is deposited off-axis, the temperature profile during the transient state becomes slightly hollow, i.e. not monotonically decreasing with increasing ρ. This behaviour can be intuitively expected, however, it does not necessarily arise, which shall be explained in the following. When switching on additional ECRH power at ρ_{dep}, the electron temperature immediately starts rising at this point, forcing the temperature gradient slightly inwards of ρ_{dep} to decrease in magnitude. The temperature gradient falls below the critical temperature gradient of the critical gradient model which largely reduces transport. Heat flux coming from the very inner plasma region and crossing the flux surface at ρ_{dep} is governed by Ohmic heating and radiation losses for flux surfaces at $\rho < \rho_{\text{dep}}$. Provided that radiation is low in the centre, the Ohmic heating is large enough to – together with the small transport coefficient in the centre – keep the electron temperature profile peaked. However, for this shot the plasma current and consequently the Ohmic heating power are low whereas the impurity accumulation and therefore the radiation losses via bremsstrahlung are high. Hollow profiles therefore need to be expected in transient states where ECRH power is increased. After switching off in (b), the profile remains peaked even when the temperature in the outer regions has already decreased, since χ_e is small closer inside than the region of heating deposition, prohibiting that the information of "less heating" propagates inwards fast.

4.2.2 Radial Transport Time Scales

The next step is to determine the communication time between different plasma regions, i.e. how fast T_e reacts on changes in heating at different ρ. For this purpose the parametrisation

$$T_e(t) = T_{e,0} + H(t-t_0) \cdot \Delta T_e \cdot \left(1 - e^{-(t-t_0)/\tau}\right) \qquad (4.1)$$

is used to fit the time traces of the electron temperature channels. Assuming a constant temperature $T_e = T_0$ shortly before and an exponential growth after the power step, t_0 gives the time when the corresponding temperature channel starts reacting on ΔP_{ECRH} which is added at t_{heat}. τ is the characteristic time it takes to reach the fraction $1/e$ of the total temperature increase ΔT_e.

Figure 4.4 depicts the data points of several electron temperature channels measured by ECE for shot #34927. Temperature data when additional heating is switched on is shown in the left column, the same is on the right for switching off. The fits (full lines) using equation 4.1 are performed on a time window of 25 ms, ranging from 10 ms before heating starts to 15 ms after t_{heat}. They are done for each ECE channel separately, which cannot be related to a fixed ρ due to a shift in the plasma, called *Shafranov shift* which is caused by the increase of the plasma energy. However, the spatial deviation is within a few percent over the fit interval and lies within the measurement uncertainties of the ECE diagnostic.

The radial profiles of the fit parameters $T_{e,0}$, ΔT_e and τ as well as the radial transport time $t_0 - t_{heat}$ are plotted in figure 4.5. All fits where the standard deviation of one of the parameters exceeds 0.7 times its own value are not shown. The original temperature profiles in stationary state are well reconstructed in (a). The difference in temperature due to changed heating power is shown in (b). ΔT_e for switching off seems to be larger than for switching on, however, this is due to only considering a limited time window of 15 ms. The temperature channels close to the plasma edge react with a time delay of approximately 3 ms on changes in heating at $\rho = 0.26$. This behaviour is depicted in (c) where the onset of the temperature rise in relation to the time when heating starts is plotted. The negative values for the inner radii are artefacts of the fitting and give an indication of the uncertainties. The characteristic time for the temperature rise is given in (d). It is smallest at the deposition radius and increases outwards and inwards, whereas inwards it is much larger. This tendency is
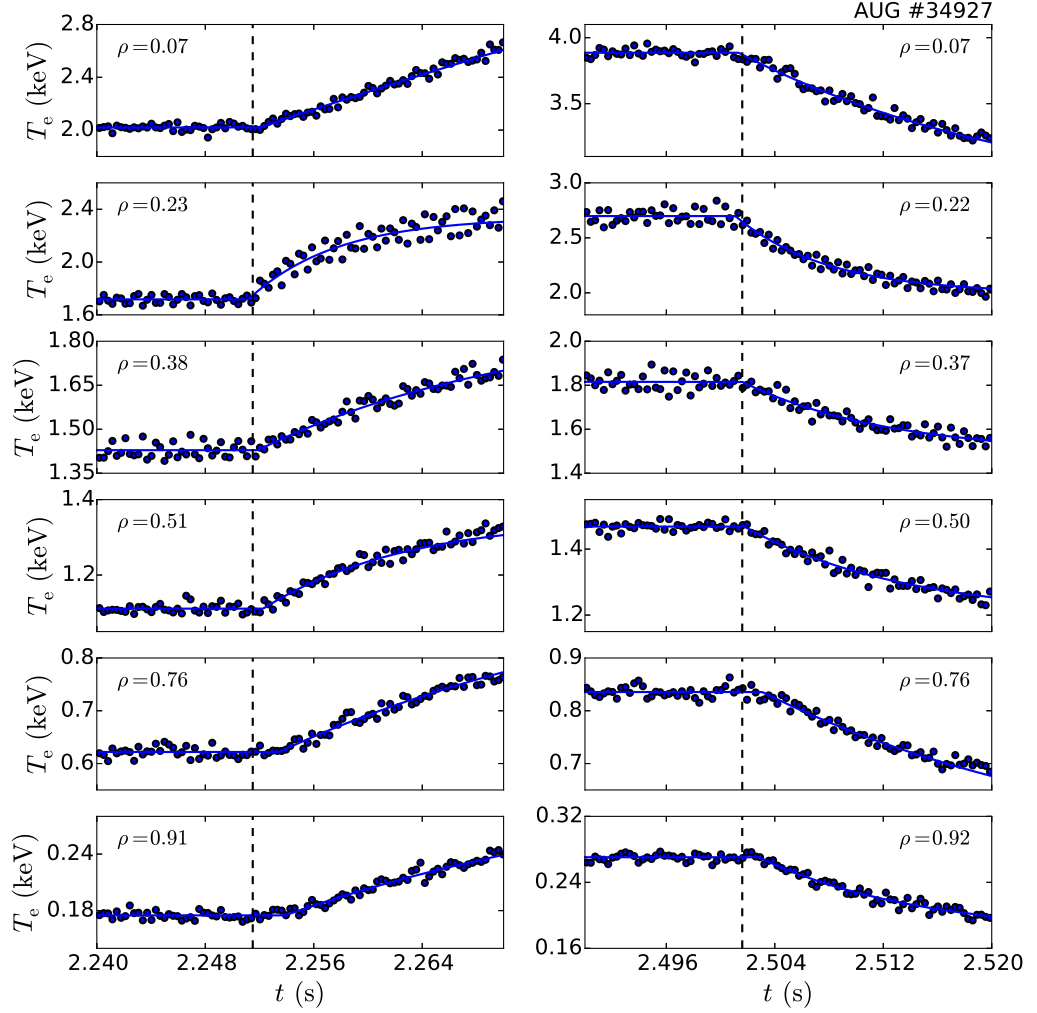
Figure 4.4: Temporal evolution of the electron temperature at different radii while adding (left) and removing (right) ECRH power. Dots: ECE measurement data, lines: fits according to equation 4.1.

based on the value of the transport coefficient which is low inside and high outside ρ_{dep} according to the critical gradient model.
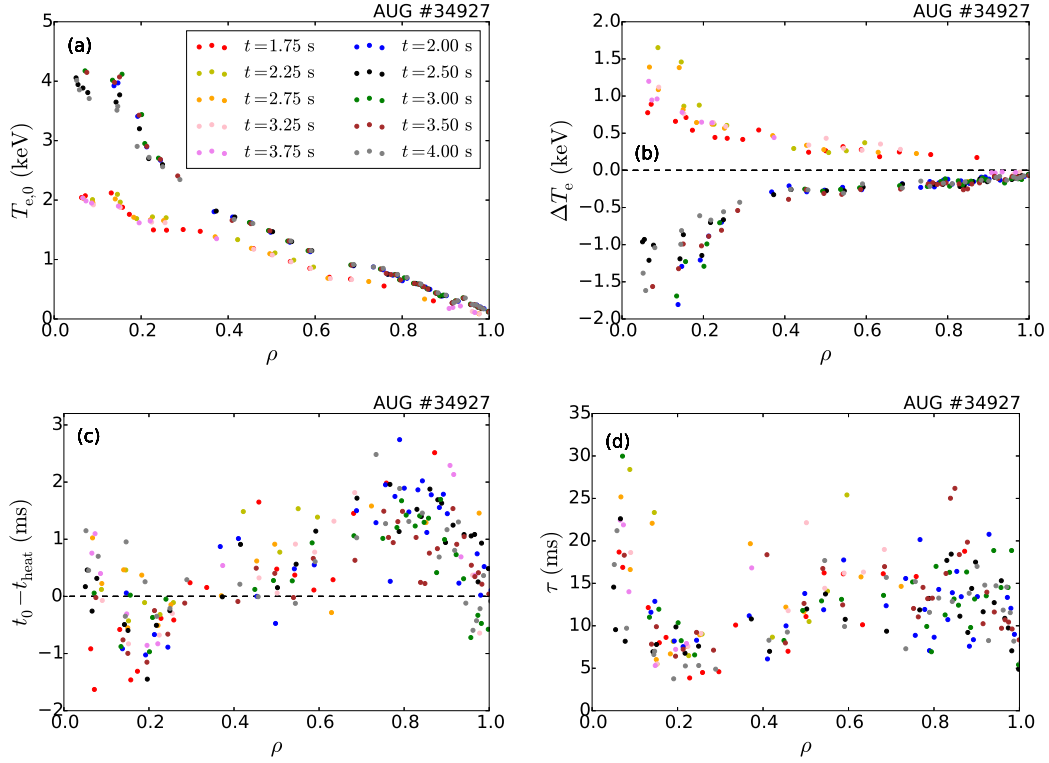
Figure 4.5: Profiles of the fit parameters from equation 4.1 used to describe the temporal evolution for the temperature at different ρ after suddenly increasing (bright colours) and decreasing (dark colours) ECRH power.

4.2.3 Electron Temperature Gradient

According to Fick's law the temperature gradient is directly related to the heat flux. Therefore ∇T_e is carefully calculated in this section to enable reliable analyses using this data later.

The noise of the raw temperature data prohibits a direct calculation of the spatial derivative, so two different approaches to treat them before deriving are examined here. One method is to fit the data by an adequate function which can then be analytically derived. Another possibility is to smooth over a certain spatial range and calculate the gradient as

$$\nabla T_\mathrm{e}(R_\mathrm{n}(\rho)) = \frac{1}{N} \cdot \Sigma_{\mathrm{i}=1}^{N} \frac{T_\mathrm{e}(R_\mathrm{n+i}) - T_\mathrm{e}(R_\mathrm{n-i})}{R_\mathrm{n+i} - R_\mathrm{n-i}} \tag{4.2}$$
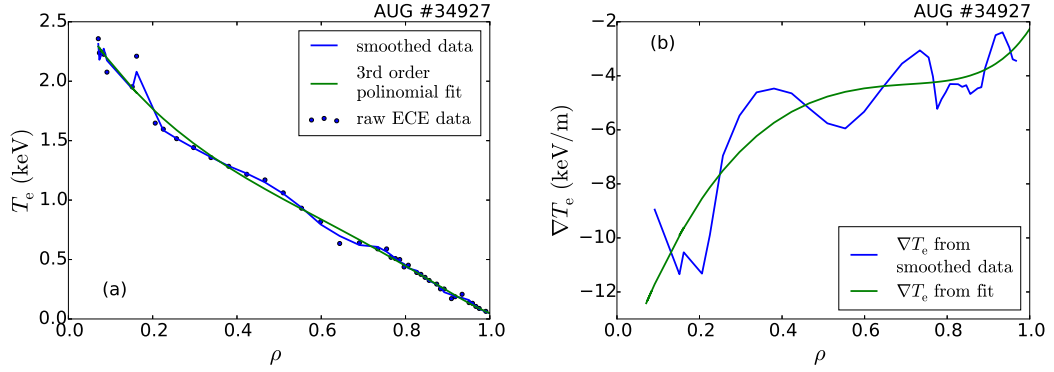
Figure 4.6: T_e profiles (a) and the corresponding ∇T_e profiles (b) at $t = 2.6$ s.

where R is the major radius of the point where the flux surface crosses the magnetic axis on the low field side, N an arbitrary small natural number (> 0) and n the lattice number in the grid. For the study of non-local transport special care has to be taken to find ∇T_e as according to perfectly local transport, the plasma quantities and their gradients at one position determine the transport at this position, but transport on all other positions is independent of that. Radially smoothing the measured values means a smearing of experimental data which could indicate non-locality, that in fact originates from the evaluation process.

In order to keep the channels widely independent and therefore leave the data local, but on the other hand provide reliable data for the spatial derivative, a meaningful number of points for spatial smoothing is 5, ($N = 2$). Before smoothing, the ECE data is interpolated on a grid with 160 radial points of constant distance, as the distance between different ECE channels is variable which would distort the smoothing. Afterwards it is interpolated back to the original radial locations. Fitting a polynomial function not only strongly induces a seemingly non-locality, but also neglects smaller structures, so it shall be just shortly shown for comparison.

Figure 4.6 (a) depicts the raw ECE data (blue points) with the smoothed ECE data (blue) and a third order polynomial fit for comparison (green). The corresponding temperature gradients are plotted in (b). For further analyses the temperature gradient determined using the smoothed ECE data will be used as it imposes less coupling between the channels than a fit and therefore allows more reliable investigations about non-local transport.
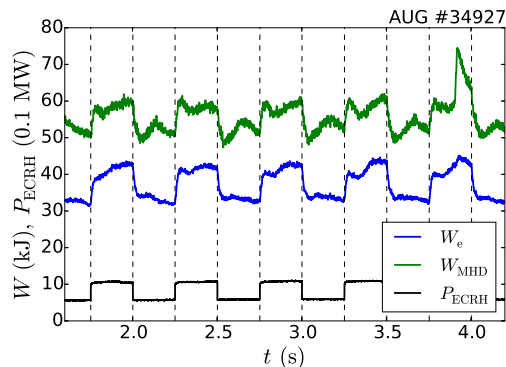
Figure 4.7: Integrated total electron plasma energy W_e compared to the total plasma energy from magnetics W_{MHD}.

4.3 Electron Power Balance Equation

All terms which are used to evaluate the electron heat flux from the power balance equation (equation 2.15) are reported on in this section. The first part, the time derivative of the internal electron plasma energy, requires most attention. It is followed by a comparison of heating power and radiated power, as well as the power transferred to ions via electron-ion interactions.

4.3.1 Internal Electron Energy

The kinetic energy of the electrons is obtained via integration of $T_e \cdot n_e$ over the plasma volume using the Riemann sum, i.e. multiplying this product for different ρ by the volume inside thin consecutive volume shells around ρ. T_e is taken from ECE measurements, n_e from IDA, whereas the volume is calculated by the plasma equilibrium code CLISTE [29].

Figure 4.7 shows the calculated total kinetic energy of the electrons W_e (blue) and the total energy W_{MHD} (green). $W_e \approx W_{MHD}$ holds, because of strong pure electron heating via ECRH and the small energy exchange between electrons and ions due to the low plasma density. The deviation in the shown time window is strongest at $t = 3.82$ s where the NBI blip dominantly heats the ions due to a large ion scattering cross section.

With regard to plugging the plasma energy into the power balance equation, the

temporal derivative needs to be calculated. As indicated in section 4.2.3 determining the derivative of a noisy quantity requires care. Temporally smoothing the data as done radially for ∇T_{e} distorts the time trace of W_{e} in a way that its derivative becomes continuous. For a sudden change in heating the energy content inside a flux surface ρ, $W_{\mathrm{e}}(\rho)$, is expected to increase linearly from t_{heat} to t_0 and then exponentially. t_0 corresponds to the time at which $T_{\mathrm{e}}(\rho)$ starts reacting to the change in heating. The time derivative is expected to be discontinuous. After having tried several ways of determining $\dot{W}_{\mathrm{e}}$, it turned out that fitting

$$W_{\mathrm{e}}(t) = W_{\mathrm{e},0} + H(t_{\mathrm{heat}} - t_0) \cdot \Delta W_{\mathrm{e}} \cdot \left(1 - \mathrm{e}^{-(t_{\mathrm{heat}} - t_0)/\tau}\right) \tag{4.3}$$

on each radial channel gives the most reliable and accurate results even though it slightly differs from analytical predictions. Note that other than for T_{e}, t_0 is not a fitting parameter for W_{e}, but kept constant at $t_0 = t_{\mathrm{heat}}$, as discussed in section 2.5.2. Figure 4.8 shows the response of $W_{\mathrm{e}}(\rho)$ (points) and the fitted function (full line) on the power steps for various ρ. Switching on additional ECRH power is depicted on the left, switching it off on the right.

Deviations between the calculated data and the fit function arise at radii further out, where shortly after t_{heat} the energy is predicted to rise linearly instead of exponentially. By fitting the exponential function, the magnitude of the true slope is overestimated in a short time interval after t_{heat}. Due to fast time scale changes in W_{e}, this deviation can not clearly be seen in figure 4.8. In case the linear rise shall be taken into account, it has to be added to the fit function as fit parameter because the linear rise time is not known. In total three more fit parameters would be included which increases the degrees of freedom so that also small time scale structures are taken into account which do not origin from the change in heating power. In order to handle this problem one could assume the linear rise time to be the same as the time it takes the temperature to react on the power step, however, this would a priori exclude one signature of non-local transport and is therefore not valid in this analysis. The noise of the data does not allow this effect to be taken into account reasonably. The time window used for fitting is 10 ms before until 15 ms after t_{heat}. The time derivatives of the plasma energies depicted in figure 4.8 are shown in figure 4.9. As uncertainties of both, T_{e} and n_{e} are propagated to W_{e} and its derivative, $\dot{W}_{\mathrm{e}}$ will be the contribution to the power balance equation with the largest uncertainties.
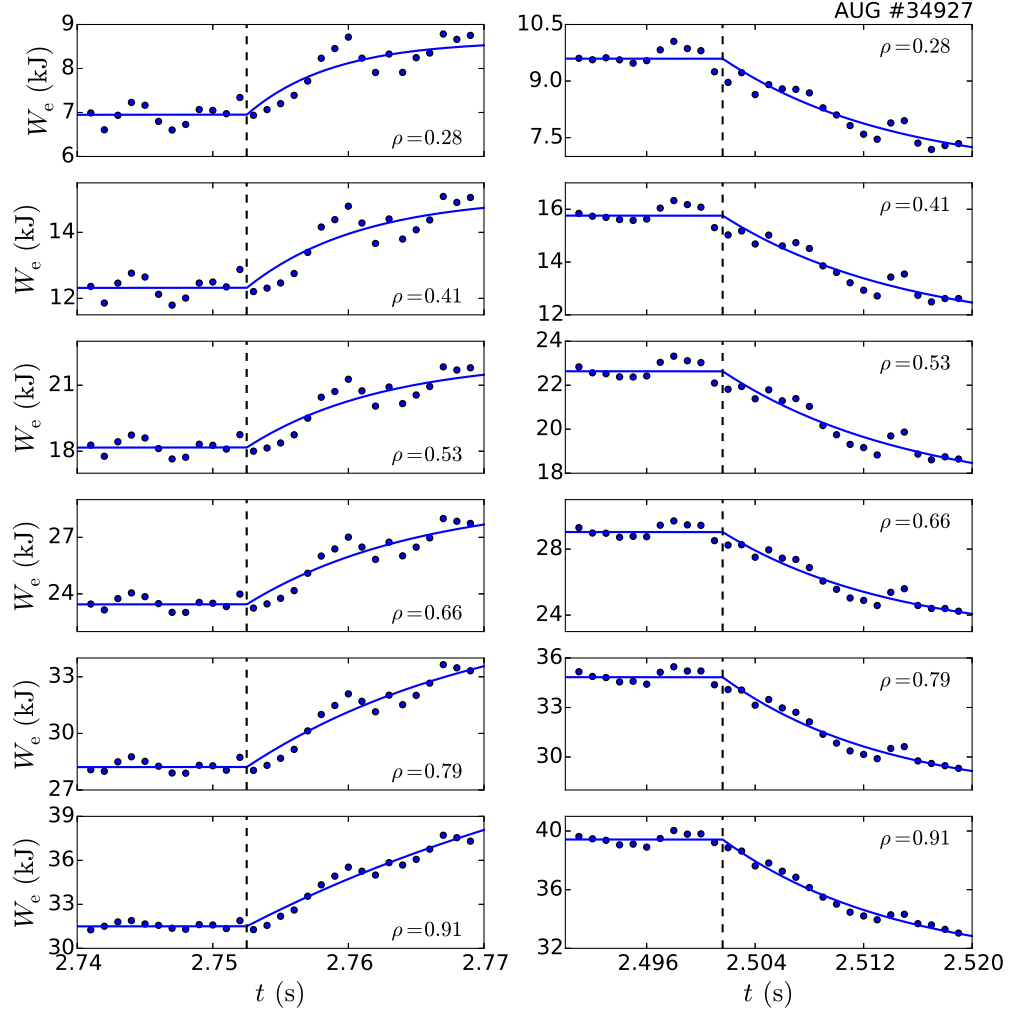
Figure 4.8: Evolution of the electron plasma energy W_e inside different flux surfaces while switching on (a) and off (b) ECRH power. Dots: data from integration, lines: fits according to equation 4.3.

In figure 4.10 the parameters used for fitting the evolution of the electron energy are plotted over ρ. The initial profiles $W_{e,0}$ (a) are highly reproducible and the differences ΔW_e (b) show an unambiguous tendency as well. The characteristic rise
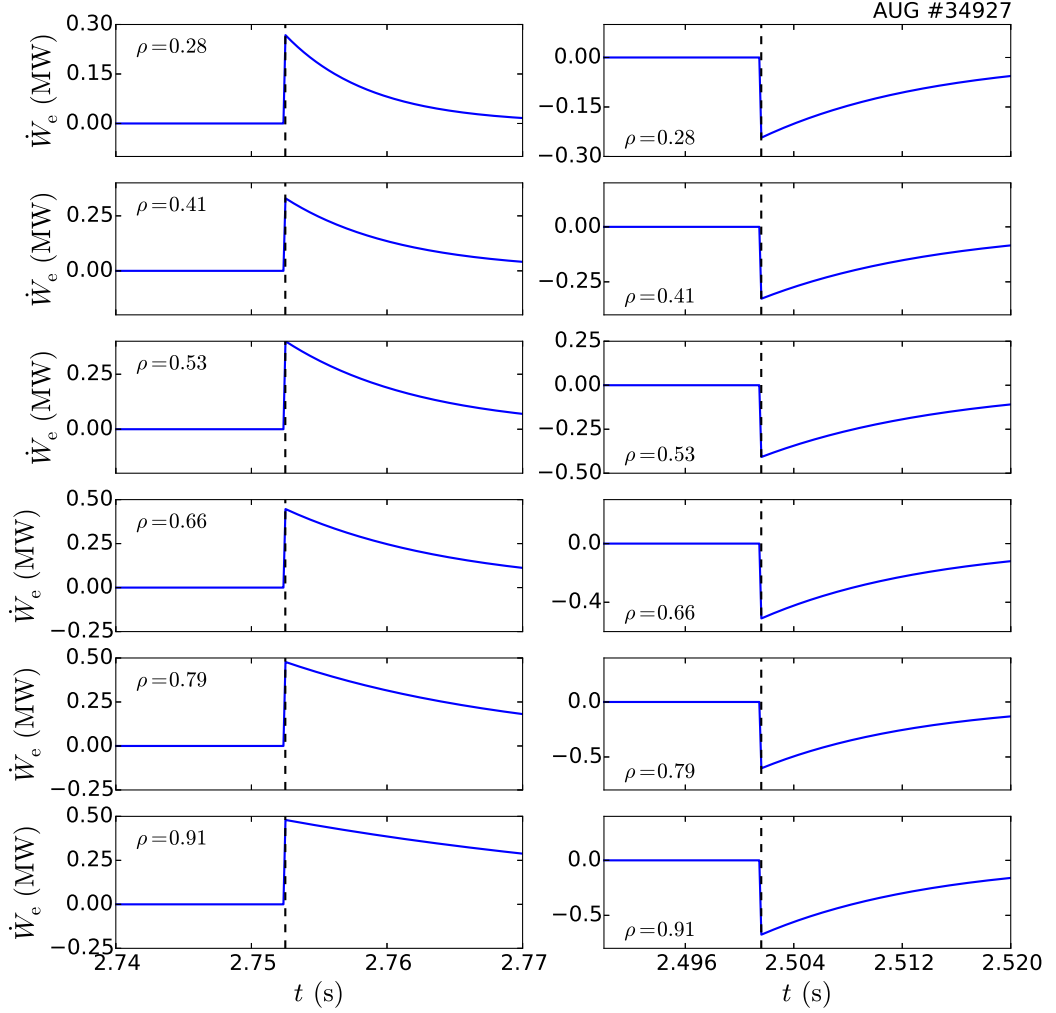
Figure 4.9: Time derivative of the electron plasma energy for different radii, obtained by fitting an exponential function (equation 4.3) to the electron energy data.

and fall time τ lies in the same range as for the electron temperature (≈ 10 ms) and increases with increasing radius, owing to the already mentioned fact that one flux surface cannot be in stationary state before the flux surface closer to heating deposition has reached stationary state. As done in section 4.2.2, all parameter-sets
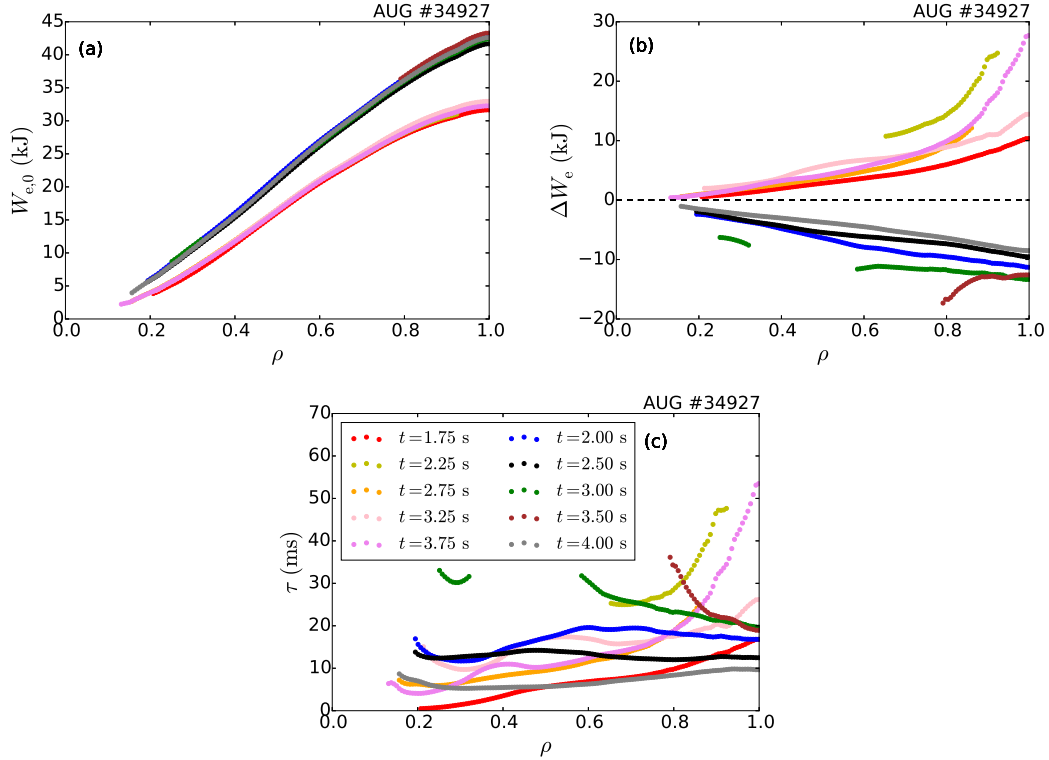
Figure 4.10: Profiles of the parameters from equation 4.3 used to fit the electron energy enclosed by a magnetic flux surface responding to a change in ECRH power. Switching on in bright colours and switching off in dark colours.

where the standard deviation of at least one parameter exceeds its own value times 0.7 are left out.

4.3.2 ECRH Power, Ohmic Power and Radiated Power

In the context of this thesis the ECRH power density (power per volume) is calculated by the code TORBEAM [30]. The Ohmic power density is computed by the code TRANSP [31], using the neoclassical resistivity which takes into account the geometry of the magnetic field, but neglects fluctuations. Amongst others the Ohmic power depends on the effective mass number of the plasma ions, Z_{eff}, which is assumed here to be 1.8. Several bolometer lines of sight [32] measure the radiated power.

Figure 4.11 (a) and (b) depict the spatial profiles of the ECRH and Ohmic power density deposition and the radiated power density emission for both, the stationary state with high heating power (a) at $t = 2.499$ s and low heating power (b) at $t = 2.249$ s. The ECR heating takes place very locally in radius, its deposition regions is Gaussian distributed. The Ohmic power density is largest close to the magnetic axis as this is the place where most of the plasma current flows when the temperature profile is peaked. Due to the temperature dependence of the resistivity it decreases for adding and increases for removing ECRH power in order to keep the plasma current constant. In the experiments performed for this thesis the radiated power is low compared to average plasma discharges done at ASDEX Upgrade. Thus the absolute radiation value is just slightly above the noise level of the measurement and the transient states after switching ECRH power cannot be reproduced. However, spatially resolved bolometer data is available for stationary states, whereas for P_{rad} a stationary state is assumed to start 50 ms after the ECRH step and end at the onset of the next ECRH step. The radiated power within these 200 ms is constant over time, P_{rad} in the transient state (50 ms) is assumed to be a linear interpolation between the two neighbouring stationary states. The total power deposited and emitted inside a flux surface at ρ is shown in (c) for the high power stationary state ($t = 2.499$ s) and in (d) for the low power stationary state ($t = 2.249$ s). As designed for electron transport studies the ECRH power is the dominant term. At high heating power in (d), the radiated power more than doubles, compared to (c), whereas the Ohmic heating power and its change are small in absolute numbers.

4.3.3 Electron-Ion Energy Exchange Term

The energy exchange between electrons and ions requires careful calculations and precise T_{e} and T_{i} profiles to be accurately determined. However, in the context of this thesis its exact value is not necessary to have in case it is small and/or does not change a lot during the transient phases of ECRH power steps. This section shall prove true both of these conditions, by comparing the time evolution of the ion temperature to the time evolution of the electron temperature for different magnitudes in ECRH power. In the time interval under consideration n_{e} and n_{i} almost stay constant. Hence, from the temporal change in temperature direct conclusions can be drawn on the electron-ion energy exchange term.
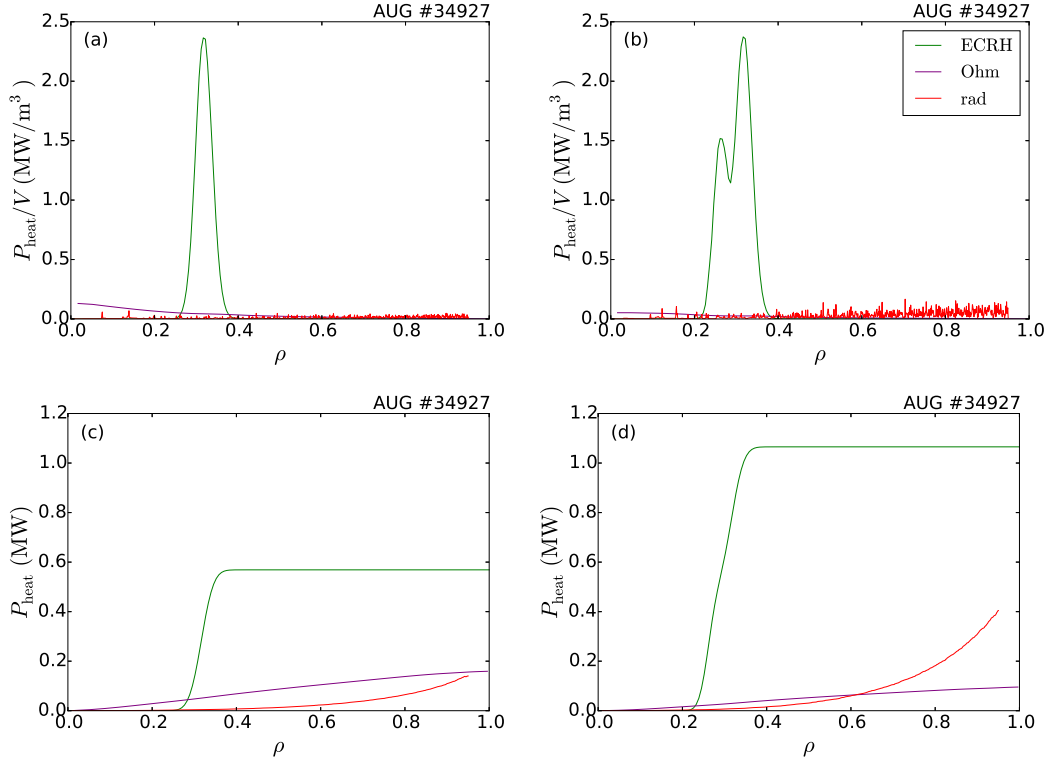
Figure 4.11: Radial profiles of ECRH, Ohmic and radiated power deposition/emission density in (a),(b) and enclosed power in (c),(d) for a low power stationary state ($t = 2.249$ s) in (a),(c) and a high power stationary state ($t = 2.499$ s) in (b),(d).

A third experimental scenario exists in the context of this thesis, which is of interest in this section. Several ECRH power steps of different magnitudes are performed on top of a background gyrotron. After each switching process, an NBI beam blip provides a time window of 16 ms for ion temperature measurements with the charge exchange diagnostic. Figure 4.12 (a) shows T_i for different radii and the ECRH and NBI power. As a large fraction of the injected NBI power heats the ions, the ion temperature increases during one blip and then equilibrates back to its original value. T_i and its rise are to a large degree independent of the heating put into the electrons and the much larger electron temperature. Figure 4.12 (b) shows representative ion temperature profiles measured by charge exchange at three time points in comparison to the corresponding electron temperature profiles measured by ECE. These plots
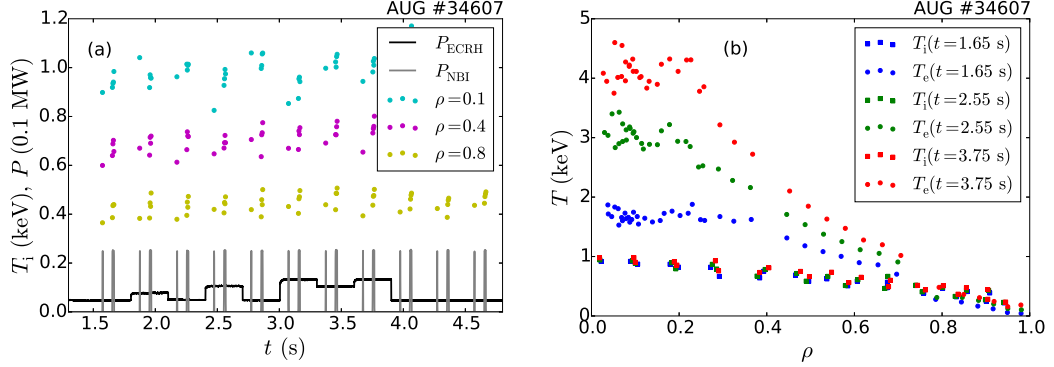
Figure 4.12: T_i at different ρ over time and the plasma heating sequence in (a), T_i and T_e profiles at different time points in (b).

confirm that the electron and ion heat channels are only weakly coupled and that the energy exchange term is negligible for the analysis presented here.

4.4 Electron Heat Transport in the Transient State

In the following, the data discussed in the previous sections are combined and the power flux q_e is calculated as a function of time and radius using equation 2.19. A conclusion from this chapter is that transport points to being local for the experiments considered here.

4.4.1 Power Flux from the Power Balance Equation

The power $Q_e(\rho)$ flowing through one magnetic flux surface arises from the power balance equation and is in this section calculated as (see equation 2.15)

$$Q_e(\rho) = P_{\mathrm{ECRH}}(\rho) + P_{\mathrm{Ohm}}(\rho) - P_{\mathrm{rad}}(\rho) - \frac{\mathrm{d}W_e}{\mathrm{d}t}(\rho). \qquad (4.4)$$

All terms correspond to the power deposited, absorbed and emitted, respectively, inside a magnetic flux surface. Figure 4.13 (a) shows the power flow $Q_e(\rho = 0.6)$ as well as the quantities from which it is calculated. When additional ECRH power ΔP_{ECRH} (green) is added at ρ_{dep} inside $\rho = 0.6 > \rho_{\mathrm{dep}}$, the plasma energy inside $\rho = 0.6$ immediately starts rising. $T_e(\rho = 0.6)$ and $\nabla T_e(\rho = 0.6)$ remain constant

until the heat pulse coming from ρ_{dep} reaches $\rho = 0.6$ which takes a few milliseconds (c.f. figure 4.4). During this time the power flowing through the flux surface is still the same as without additional heating power, causing ΔP_{ECRH} to be fully absorbed by the electron energy which rises linearly (neglecting radiation). As the heat pulse reaches $\rho = 0.6$, i.e. $T_{\text{e}}(\rho = 0.6)$ starts rising, the heating power stops solely feeding the internal energy and is partially transported outwards as power flux. The electron energy rises slower than before, the evolution equals an exponential function (c.f. equation 4.3). The linear rise lasts for 1–2 ms after changing heating, which for data with a time resolution of 1 ms means that the reaction of W_{e} to heating can be assumed to immediately be exponentially (c.f. section 4.3.1). As predicted from these argumentations (which are based on local transport), the time derivative of the experimentally measured electron energy (dark blue in figure 4.13) compensates the power step, whereas Q_{e} continuously rises and reaches a constant value stationary state (not shown). $\dot{W}_{\text{e}}(t > t_{\text{heat}} + 15\text{ ms})$ is the difference quotient of temporally smoothed W_{e} data. Following the discussions in section 4.3.2, for $\Delta P_{\text{ECRH}} > 0$ the Ohmic power (purple) decreases at constant plasma current, whereas the radiated power (red) increases due to a larger impurity accumulation. Referring to section 4.3.3, the electron-ion exchange term is left out completely.

Figure 4.13 shows the reversed process for the flux surface at $\rho = 0.6$ where ECRH power is removed at $\rho_{\text{dep}} = 0.26$. Until the cold pulse reaches $\rho = 0.6$, the electron temperature gradient at this position remains unchanged. Within this time Q_{e} remains constant and is fed by the plasma energy enclosed by $\rho = 0.6$ which needs to rapidly decrease to come up for the former heating power. As after 1–2 ms $\nabla T_{\text{e}}(\rho = 0.6)$ starts decreasing, the heat flux becomes smaller, allowing $W_{\text{e}}(\rho = 0.6)$ to change more slowly, i.e. causing its time derivative to become less negative. Stationary state is reached when $\dot{W}_{\text{e}}(\rho = 0.6) \approx 0$ (not shown). Following the argumentations for (a), P_{Ohm} rises to keep I_{P} constant, P_{rad} decreases due to a smaller impurity density and $P_{\text{e,i}}$ is neglected.

The next step is to calculate Q_{e} as a function of time and space. Figure 4.14 depicts the time evolution of $q_{\text{e}} = Q_{\text{e}}/S$ for different radial points ρ. As discussed in section 4.3.1 the time derivative of W_{e} is inaccurate a few milliseconds after the power step as the slope of the electron energy is slightly overestimated due to the chosen fit function. The effect is largest near to the edge as the enclosed energy first increases
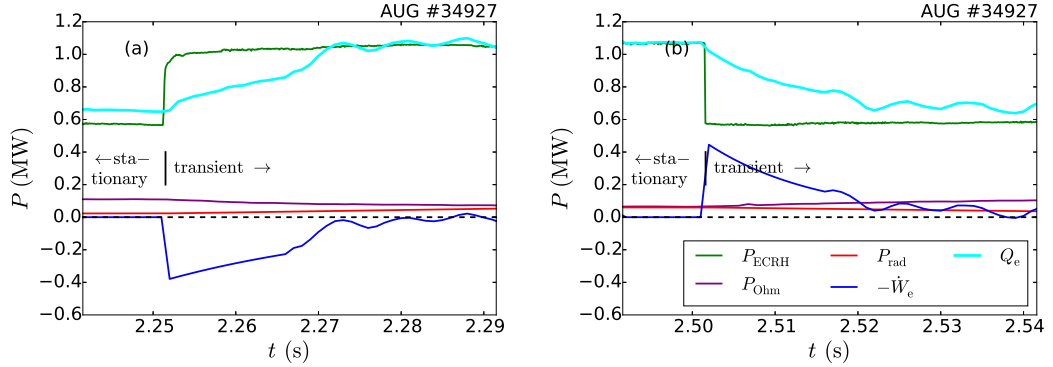
Figure 4.13: Visualisation of all terms contributing to the electron power balance inside the flux surface $\rho = 0.6$ for switching ECRH on (a) and off (b). The power flowing over one flux surface is the sum of all plotted quantities.

linearly until the corresponding local temperature starts rising, which lasts longest far away from the area of heating deposition, i.e. in the edge. This overestimation propagates into the estimation of q_e which in a short time window seems to behave opposite than expected.

Due to these uncertainties no statement about about a jump in the power flux can be given. After an ECRH power change, q_e changes smoothly (especially in the inner plasma region). The time it takes the heat pulse to be detected in the plasma edge as increased power flux cannot be extracted from figure 4.14 with sufficient accuracy. Therefore no significant conclusion can be drawn if $\nabla T_e(\rho = 1)$ and $q_e(\rho = 1)$ react to central heating after the same time (local transport) or if there are deviations (non-local transport).

4.4.2 Power Flux and Temperature Gradient

Section 2.4 discussed that q_e emerges from the power balance equation and (via the transport coefficient and Fick's law) corresponds to a certain temperature gradient. Figure 4.15 plots the profiles of q_e and ∇T_e responding to a sudden increase in ECRH power in (a) and (c) and a sudden decrease in (b) and (d). The blue lines correspond to the stationary states, the coloured lines show the profiles at different times after switching on or off, respectively. For both, the power flux and the temperature gradient, the changes are largest close to ρ_{dep}, whereas in the edge they are small.
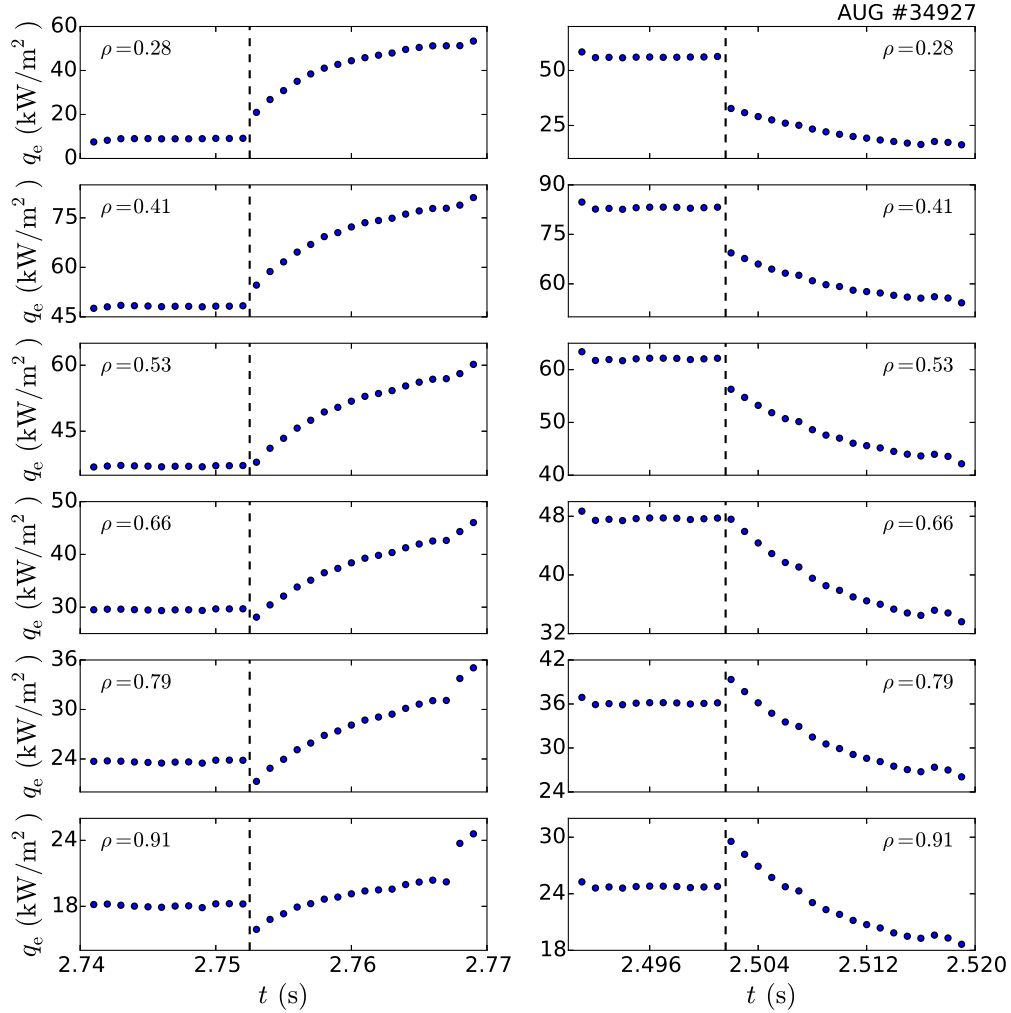
Figure 4.14: Temporal evolution of the power flux at different magnetic flux surfaces while stepwise increasing (a) and decreasing (b) ECRH power.

After 5 ms (green line), the plasma within $\rho = 0.15$ is still in stationary state, causing the little bump. Negative values of q_e arise from the power balance equation and correspond to power flowing inwards. The temperature gradient in the central region
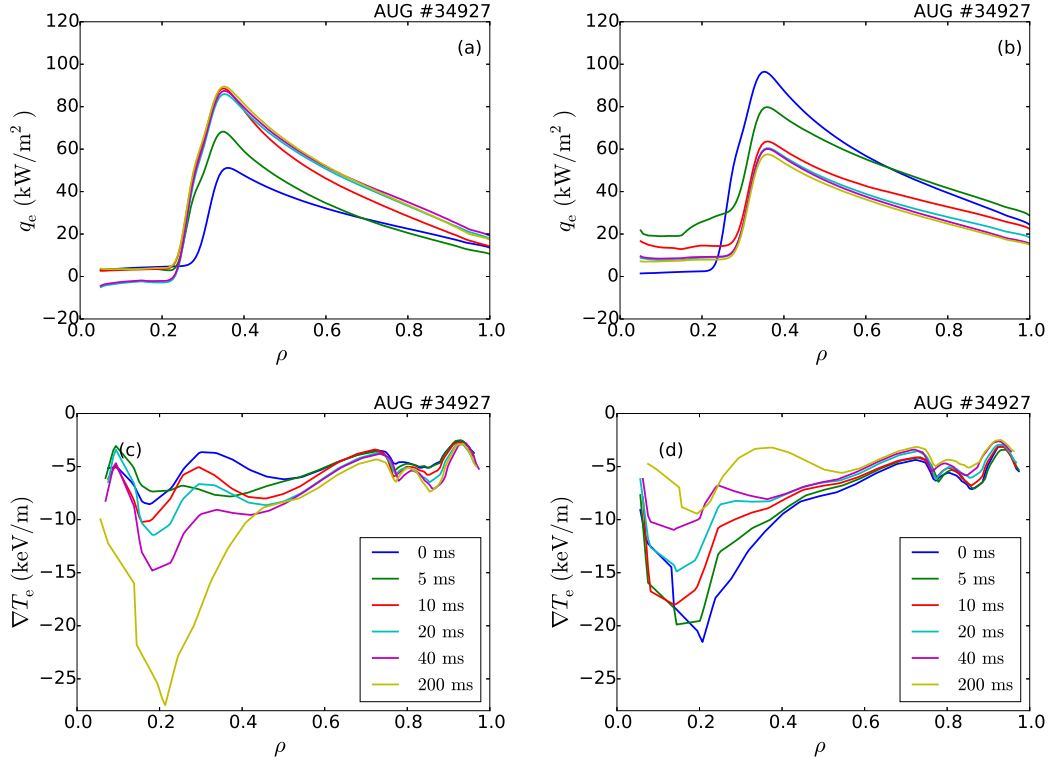
Figure 4.15: q_e and ∇T_e profile evolution for increasing (a),(c) and decreasing (b),(d) ECRH power at $t = 1.75$ s and $t = 4.00$ s, respectively.

$\rho < 0.2$ is imposed to large uncertainties due to unfavourable positioning of the ECE channels and shall not be discussed.

Outside ρ_{dep} figure 4.15 (a) and (b) show a radially decreasing power flux for the following reasons: first, the area of each magnetic flux surface increases with increasing radius, so the same amount of power flowing over each of them results in a smaller energy flux per area. Second, radiation acts as power sink as well and leaves less power to be carried for radii further out. Third, if the system is not yet in stationary state, also the electron energy acts as power sink. The time until the equilibrium temperature is reached increases with increasing radius, as the temperature on one flux surface can only reach stationary state if the flux surface closer to the heating deposition has reached stationary state before.

Following [18], [19] and [20] the flux-gradient relation is plotted for different radii

in figure 4.16 in order to search for hysteresis patterns reported in these articles. The axes are scaled following Fick's law, so that the slopes of lines going from the origin to each of the points correspond to the electron transport coefficient χ_e. The horizontal axis measures the inverse of the gradient length and the vertical axis the power flux normalised by the local density and temperature. Each plot consists of seven curves with 1 ms time resolution, stemming from consecutive 250 ms time windows, out of which three represent the measurement data after ECRH switching on (bright colours) and four correspond to the time after ECRH switching off (dark colours). In stationary state all points lay in the same region, indicated by two large clouds. Their horizontal and vertical expansion give an estimate of the uncertainties stemming from both the measurements and the evaluation. The data points from the transient states connect the two regions of stationary state, however they are hardly visible in figure 4.16. Note that, as the electron temperature gradient over electron temperature is plotted on the horizontal axis, other than the gradient alone, the high-ECRH power data cloud (bright) does not necessarily have to be to the upper left of the low-ECRH power cloud (dark).

Figure 4.17 depicts the mean values of the data of figure 4.16. The former three curves for "ECRH on" are represented by one trajectory in a bright colour, whereas the former four curves for "ECRH off" become one curve in a dark colour. Each colour pair is related to a different magnetic flux surface. Some representative points show error bars which correspond to the standard deviation of the averaging process. They however might underestimate measurement uncertainties which are better visible in the expansion of the point clouds in stationary state (in an ideal case, stationary state is represented by one point). After averaging the transient states , i.e. the two paths connecting the clouds, are visible. For both, figures 4.16 and 4.17, the points from the time window 3 ms before and after t_{heat} are left out, due to the uncertain determination of $\dot{W}_e$ and q_e in this interval. No sign of a hysteresis can be found within the error bars.

In case of having had a hysteresis effect, it could have been related to a time dependent transport coefficient. Following the gyro-Bohm hypothesis and results from gyro-kinetic calculations, the critical gradient model expects χ_e to be a function of various local quantities (c.f. equation 2.21). In the experiments under investigation, the local electron temperature strongly varies with respect to time, the local safety
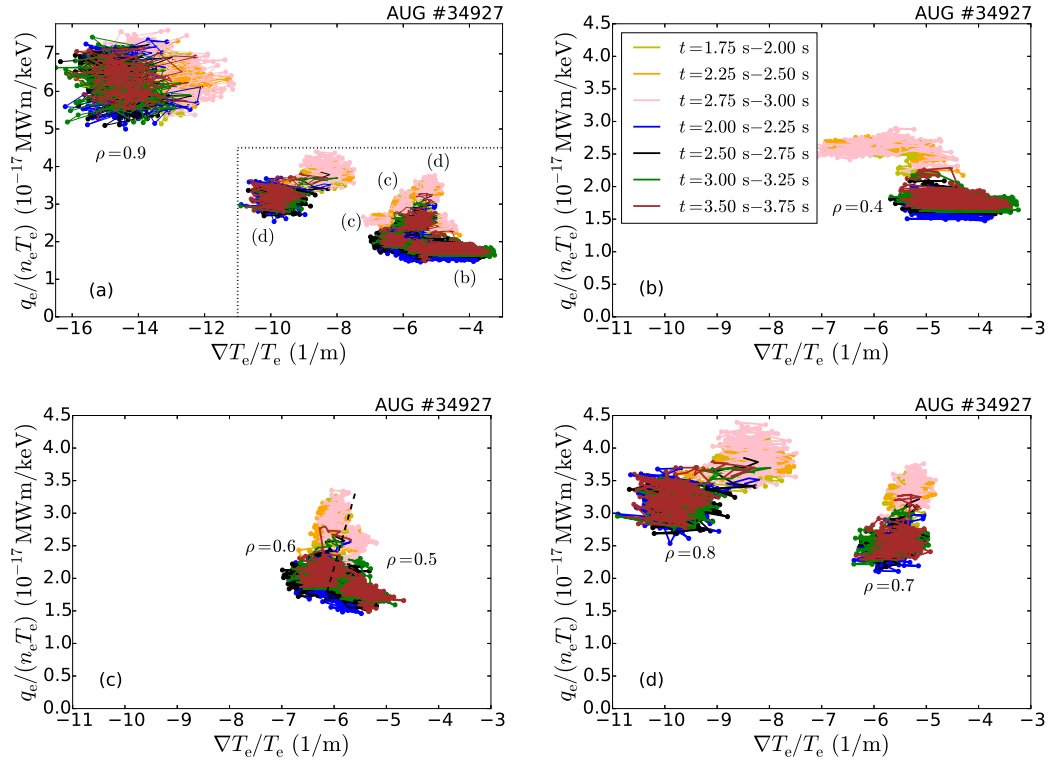
Figure 4.16: Electron power flux divided by electron density and electron temperature over the inverse electron temperature gradient length, for several time points (1 ms resolution) and radii (in different plots) while switching on (bright colours) and off (dark colours) ECRH power.

factor is to a large degree constant in the time window under investigation (c.f. section 5.2). The crucial relation in the context of this analysis is that χ_e is assumed to follow the gyro-Bohm scaling and thus to be proportional to $T_e^{3/2}$.

Figure 4.18 depicts the same data as figure 4.16, however, rescaled by $T_e^{3/2}$ as predicted by the gyro-Bohm scaling. If the electron heat transport follows the gyro-Bohm assumption and is determined by local quantities, any hysteresis which might have been visible in figure 4.16 or figure 4.17 is expected to then disappear. As the electron temperature is small close to the plasma edge, a larger scale for the vertical axis is needed for $\rho > 0.7$. In order to judge the hysteresis behaviour, the average over all curves for "on" and all curves for "off" is taken and plotted in figure 4.19. Within the error bars (depicting the standard deviation which arises from the aver-
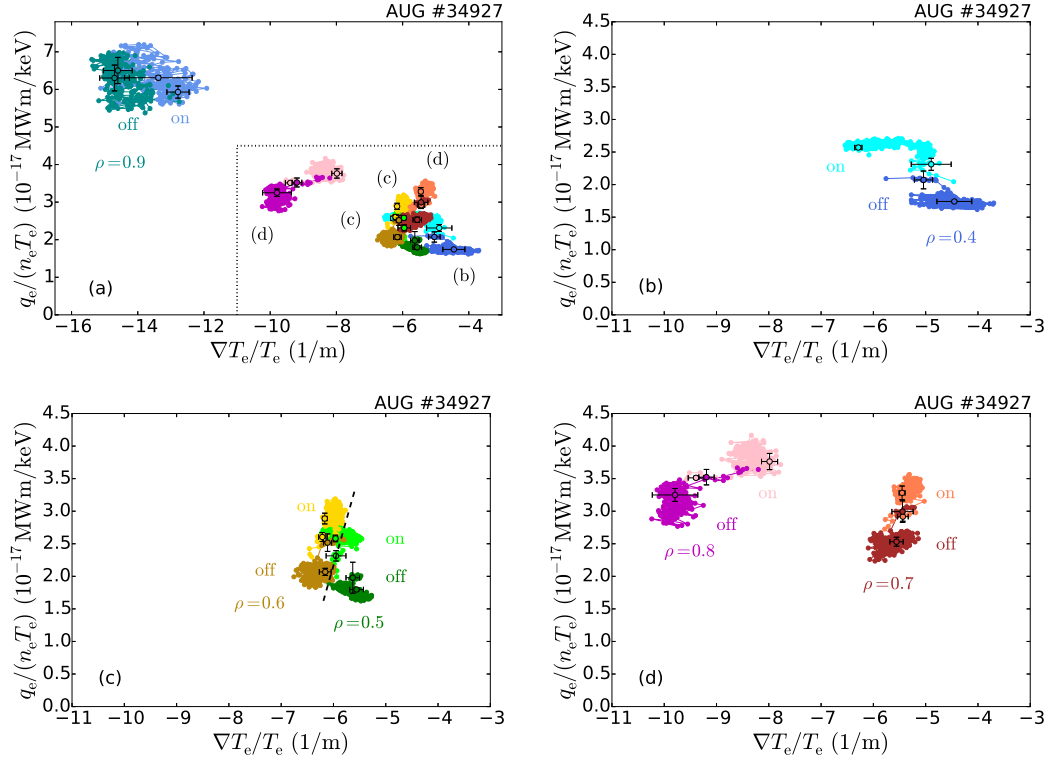
Figure 4.17: Averaged flux-gradient relation from figure 4.16, the phase after switching ECRH on in bright colours and after switching off in dark colours.

aging process) there again is an unambiguous dependence between $q_e/(n_e T_e^{5/2})$ and $\nabla T_e/T_e$.

In the following, several sources of uncertainties are discussed. First, uncertainties of the power flux are considered, second, possible inaccuracies in the temperature gradient data and third, others which are more general.

The sources of largest uncertainties of the shown data within the first couple of milliseconds after switching ECRH power is $\dot{W}_e$. This originates from the fact that it needs to be determined at the point where it is discontinuous and changes fast. However, for the hysteresis, points of $\dot{W}_e$ which are well away from t_{heat} are considered which are more accurate, as $\dot{W}_e(t > t_{heat} + 15$ ms$)$ is assumed to be the difference quotient of temporally smoothed W_e data. The analysis performed in this section is more susceptible to uncertainties coming from e.g. imprecise ρ_{dep}. Therefore only
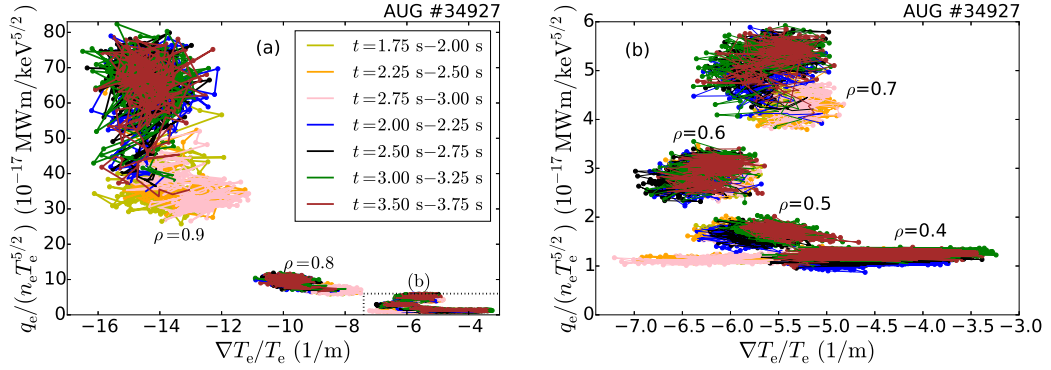
Figure 4.18: Re-scaled figure 4.16, electron power flux divided by electron density and electron temperature to the power of 5/2 over the electron gradient length in inverse meters for switching on and off ECRH power.
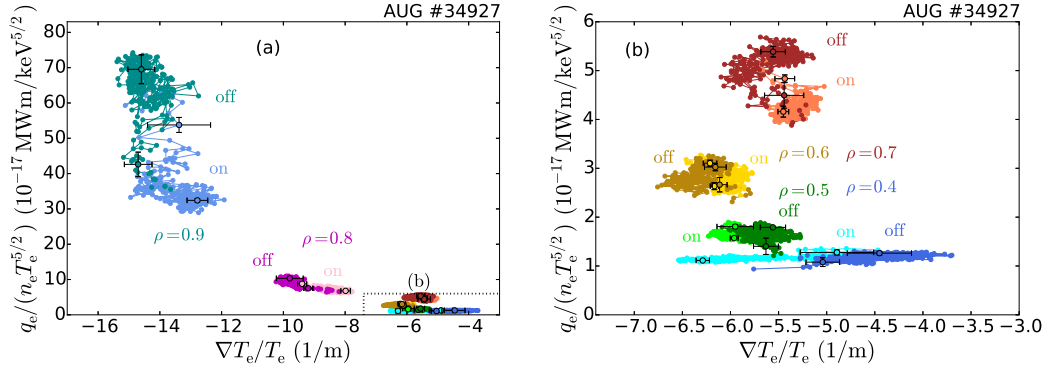

Figure 4.19: Averaged flux-gradient relation from figure 4.18, the phase after switching ECRH on in bright colours and after switching off in dark colours.

radial regions far away from heating deposition are examined. Uncertainties in P_{rad} as well as P_{Ohm} as well have an impact, where in the data discussed here, possible deviations of the first one are much larger than of the second one.

For the presented analysis, the time derivative of the kinetic energy and the spatial derivative of the electron temperature are used. As discussed in section 4.2.3, the determination of ∇T_{e} might bring artificial non-locality into the data. In order to rule out a distortion of the hysteresis due to inaccurate electron temperature gradient, many profiles at different times have been checked to ascertain a sufficient quality of
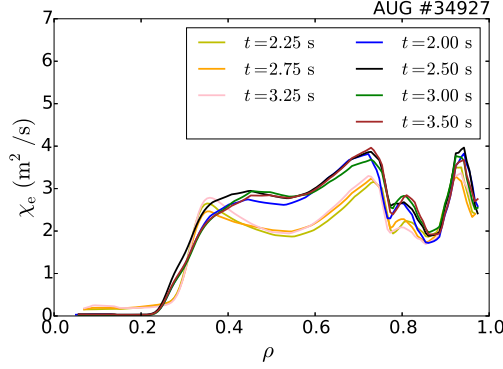
Figure 4.20: Profile of the transport coefficient in stationary state for different times, each shortly before an ECRH power step.

the spatial derivative. In case of using ∇T_e from the polynomial fit done in section 4.2.3, a significant hysteresis appears from the core up to $\rho = 0.6$ (not shown), proving that fitting can result in wrong conclusions on the existence of non-locality. Measurement uncertainties need to be considered as well. For instance, the large number of inflection points in ∇T_e may be related to the calibration of the ECE diagnostic. n_e from the IDA underlies errors of $\approx 5\%$, whereas also the equilibrium reconstruction is imposed to uncertainties. With regard to these arguments, the data of the experiments performed in the context of this thesis can be concluded to point to local transport.

4.4.3 Transport Coefficient from Power Balance and Fick's Law

Figure 4.20 depicts profiles of the transport coefficient, which is determined using equation 2.19, for the high power and the low power stationary state. The results are well reproducible, outwards transport is much faster than inwards transport, because $\chi_\mathrm{e}(\rho > \rho_\mathrm{dep}) \gg \chi_\mathrm{e}(\rho < \rho_\mathrm{dep})$. This is consistent with observations from figure 4.5 (d), where the fits on the electron temperature evolution showed a much faster rise of $T_\mathrm{e}(\rho > \rho_\mathrm{dep})$ than of $T_\mathrm{e}(\rho < \rho_\mathrm{dep})$.

The temporal evolution of χ_e for different flux surfaces is shown in figure 4.21. χ_e changes smoothly when the heating power is changed, in particular there is no sign of fast changes far away in radius from the ECRH deposition, which contradicts the non-locality observed in [16]. Close to the deposition radius there is a jump which
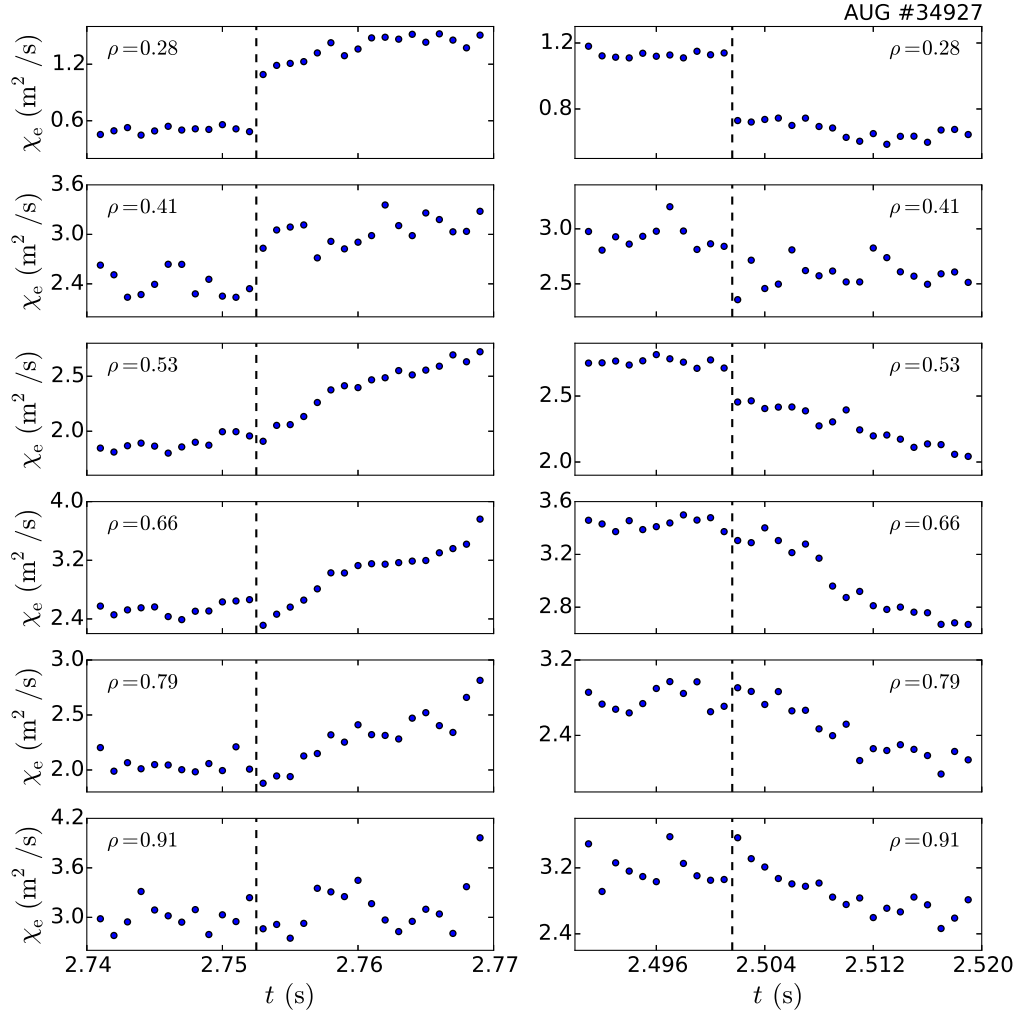
Figure 4.21: Temporal evolution of the electron transport coefficient at different magnetic flux surfaces while stepwise increasing (left) and decreasing (right) ECRH power.

originates from the fast decreasing temperature gradient and the fast increasing power flux at this position. However, following the discussion for figure 4.14, the first few ms after a power step underlie large uncertainties.

Chapter 5

Simulations for ASDEX Upgrade Experiments

This chapter examines transport simulations performed with ASTRA which are based on experimental measurements. For electron temperature profile prediction the critical gradient model is used. The main focus is the interpretation of locality or non-locality considering Fick's law, the transport coefficient and the plasma quantities the latter one depends on.

5.1 The Parameters of the Critical Gradient Model

Before using the critical gradient model for predictive simulations, three parameters need to be determined. These are the threshold "κ_{c}" in $|R\nabla T_{\mathrm{e}}/T_{\mathrm{e}}|$, above which turbulence strongly increases, the stiffness "χ_{s}" which measures the strength of this increase and a scaling parameter "χ_0" for immanently present, but low background turbulence. The region of interest is outside the ECRH power deposition radius, where the temperature gradient is well above the critical temperature gradient. Therefore χ_0 is negligible and the number of parameters reduces to two.

The method of finding them is to match experimentally measured and simulated electron temperature data by adjusting κ_{c} and χ_{s}. The experimental data comes from plasma discharge #34932 with modulated ECRH power (29 Hz). All plasma parameters such as the plasma current and the magnetic field and a temporally independent density are fed into the simulation in order to well reproduce the experiment. Only the electron temperature is calculated from ASTRA using the critical gradient model. One constraint for κ_{c} and χ_{s} is to reproduce T_{e} in stationary state.

Apart from this also the transient states need to be matched, for which the Fourier transform of the electron temperature response on ECRH modulation is considered. This is sufficient as the profiles of the amplitude $A(\rho)$ and the phase $\phi(\rho)$ at multiples of the modulation frequency give information about the propagation of heat, where both, the propagation time of the heat wave as well as its absorption by the plasma are included in $A(\rho)$ and $\phi(\rho)$. Due to simplifying assumptions, the profiles cannot be exactly reproduced. For reasonable modelling the radial dependence of the threshold is assumed to be as discussed in [12], i.e. radially decreasing, depending on the fraction of trapped particles. A reasonable value for the scaling factor of this model is 0.6. The best value obtained for the stiffness is $\chi_s = 0.6$ as well.

5.2 Simulating Power Steps

Since scenario I and II are identical apart from the heating sequence, the parameters of the critical gradient model can be assumed to be the same for both. Based on κ_c and χ_s from the previous section, the electron temperature response on ECRH power steps as done in scenario I shall be simulated. As before, the plasma density is kept constant over time and the radiated power is assumed to be zero. The time resolution is set to 0.1 ms and the period of ECRH power to 100 ms, which does not exactly match the frequency of the power steps in #34927, but still provides data close to it.

Figure 5.1 shows the simulated electron temperature response to the power steps for different radial positions in the plasma. The time the heat pulse needs to propagate outwards to the plasma edge is in the order of a few milliseconds which is consistent to experimental observations in section 4.2.2. In the context of the simulations done for this thesis, the focus is not on exactly reproducing the electron temperature data, instead the simulations should give a picture of how plasma quantities evolve with time for different radii. Therefore the absolute values of the simulated data shown here cannot be compared to the absolute values of the experimental data.

The response of the electron temperature gradient on ECRH power steps is depicted in figure 5.2. The gradient at one spatial point corresponds to the difference in temperature of the neighbouring points, divided by the spatial distance between their flux surfaces at the equatorial plane of the low field side. For $\rho = 0.3$ the change in the temperature gradient is sudden, since this is the region where the heating
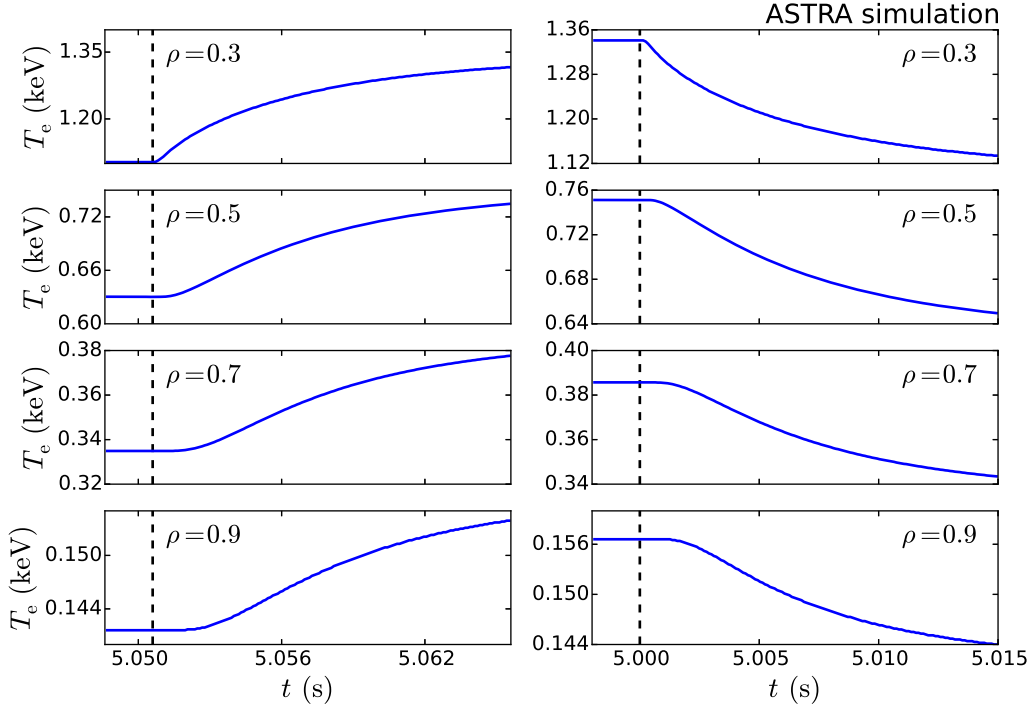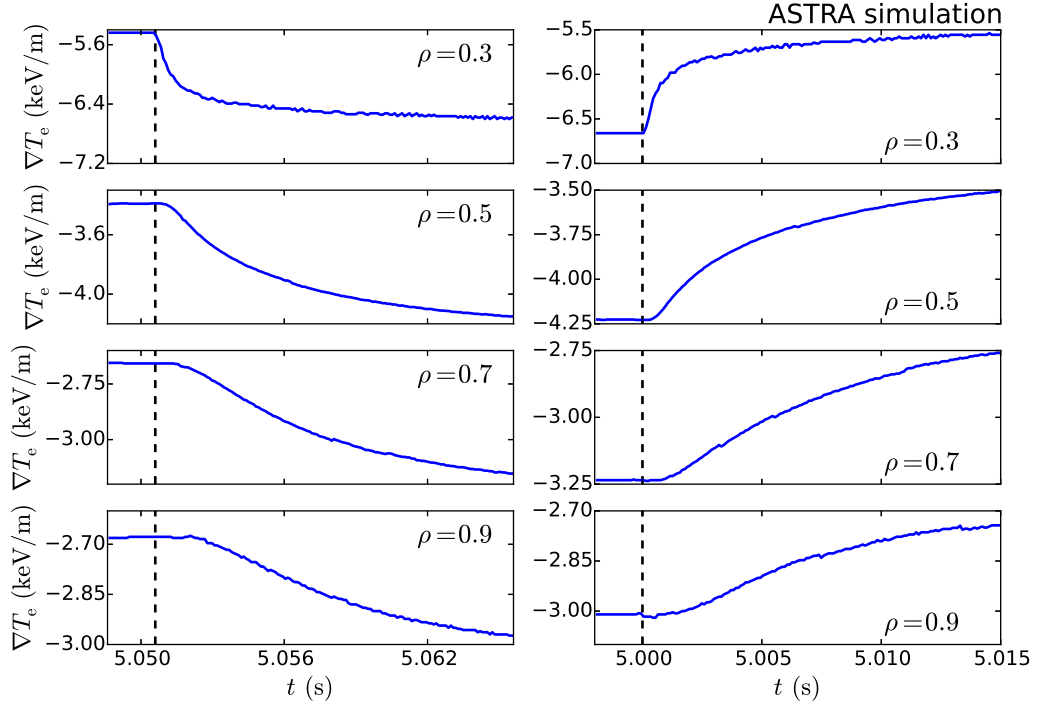
Figure 5.1: Temporal evolution of the simulated electron temperature after stepwise increasing (left) and decreasing (right) ECRH power.

power is deposited. Going further out, ∇T_e reacts later and evolves smoothly, as it takes the heatwave a couple of milliseconds to diffuse outwards. The little bumps are artefacts stemming from the technique of gradient calculation.

Figure 5.3 (a) depicts the simple flux-gradient relation directly following Fick's law, i.e. $q_\mathrm{e}/n_\mathrm{e}$ over ∇T_e (both divided by T_e to plot the inverse of the characteristic gradient length on the horizontal axis) so that the slope of the curve corresponds to χ_e. Each trajectory consists of 1000 consecutive time points at one radius. Close to the ECRH deposition area the hystereses are largest, as this is the place where the temperature changes most for different heating powers. As already mentioned, the gyro-Bohm scaling predicts the transport coefficient to be proportional to $T_\mathrm{e}^{3/2}$. Similarly to the argumentation given in the experimental data, the rescaled flux-gradient relation is shown in figure 5.3 (c), where all ambiguities disappear. Additionally con-

Figure 5.2: Temporal evolution of the simulated electron temperature gradient after stepwise increasing (left) and decreasing (right) ECRH power.

sidering the safety factor as time dependent quantity and rescaling by $q_{\mathrm{s}}^{3/2}$ gives the curves in figure 5.3 (e). They all have the same slope

$$\tilde{\chi}R = \chi_{\mathrm{s}}\frac{\sqrt{m_{\mathrm{i}}}}{e^2 B^2} \tag{5.1}$$

which, according to the critical gradient model, is neither time nor space dependent. A tiny remnant hysteresis is visible inside the region of heating deposition ($\rho = 0.3$), which shall not be discussed here as speaking of transport inside the place of power absorption requires a lot of care.

For larger heating powers the hysteresis effect becomes more pronounced (see figure 5.3 (b)). Here one background gyrotron deposits 0.5 MW at $\rho = 0.25$ and another gyrotron with a power of 1.0 MW is switched on and off at $\rho = 0.20$. As before, all hysteresis behaviour vanishes for scaling according to gyro-Bohm transport in
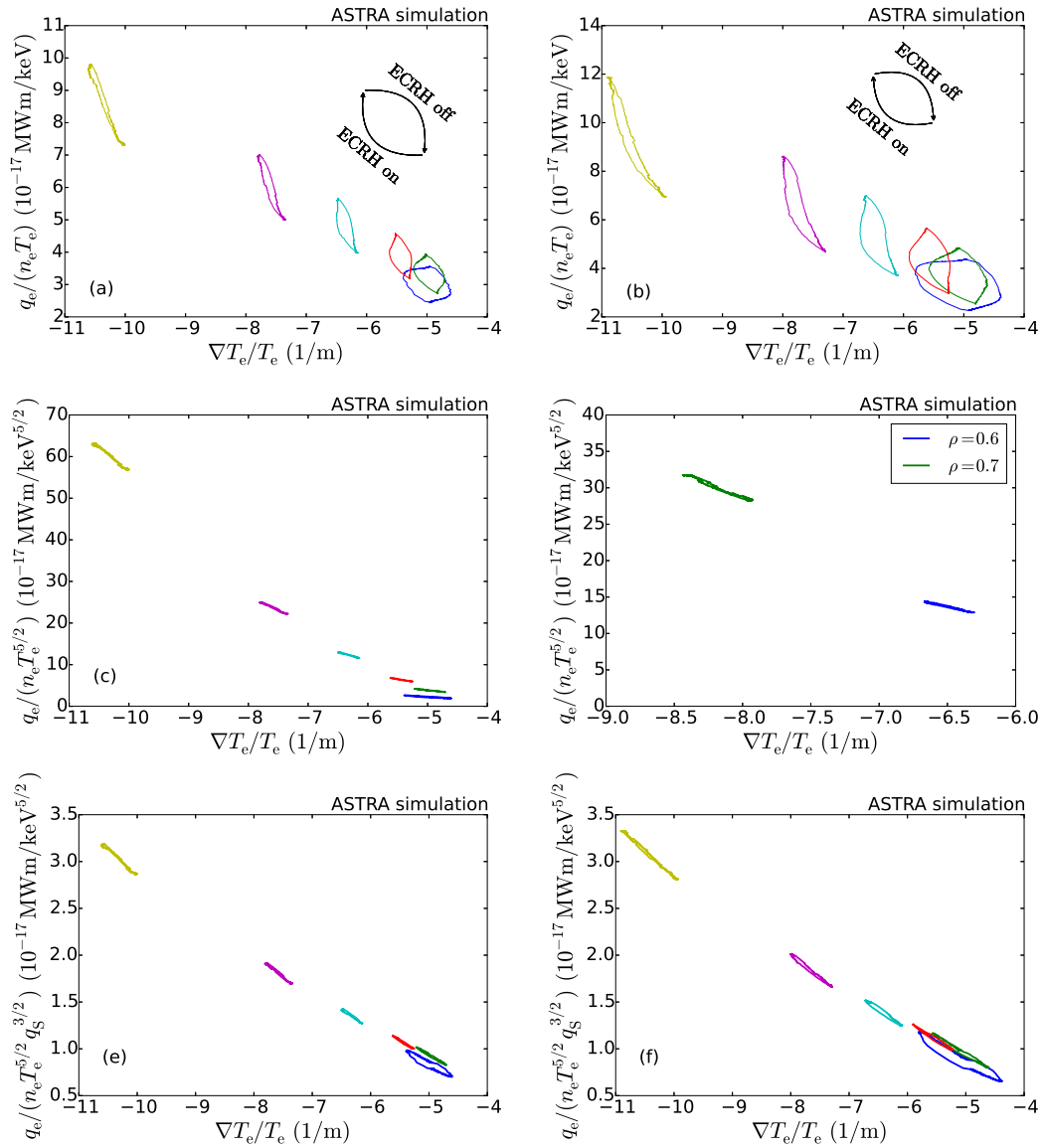
Figure 5.3: Flux gradient relation for simulated ECRH power steps analogous to discharge #34932 (a),(c),(e) and for the same plasma parameters but larger power steps (b),(d),(f). Scaling as done in Fick's law in (a),(b), scaling with the electron temperature as done in the experimental part in (c),(d) and scaling as predicted by the critical gradient model including the safety factor in (e),(f).

figure 5.3 (d). The neglected time dependence of the safety factor does not cause ambiguities, it solely leads to a different tilting of the curves at different radii, at it is a function of space. This validates having divided the experimental data by $T_e^{3/2}$ only and neglecting contributions from the safety factor. Rescaling the high power simulations by $q_s^{3/2}$ in (f) gives consistent results with (e).

Following the critical gradient model, a hysteresis in plots with axes as shown in figure 5.3 (a) and (b) and in figure 4.16 does not necessarily indicate non-locality in transport. Instead the axes need proper scaling, which then allows discussion about non-local effects in case of hysteresis behaviour. Ambiguities in (a) and (b) overwhelmingly stem from the gyro-Bohm term, for which a new scaling is given in (c) and (d), that is suffient for discussion of experimental data. The very precise way, however, would be to also include possible time dependences of the safety factor, done in (e) and (f). Still, care has to be taken when then drawing conclusions about non-local transport, in case plots as (c),(d),(e) or (f) show hysteresis behaviour, as it might stem from other transport channels like e.g. particle transport (which is neglected here as discussed in section 2.4), whereas heat transport might in fact be local.

As discussed in section 2.6, non-locality can also be detected as such if to a sudden change in heating power the transport coefficient far from heating deposition responses with a large step (c.f. [16]). In the context of the simulations also the response of the electron transport coefficient as predicted by the critical gradient model is shown in figure 5.4. The most important thing is that close to the region of ECRH deposition the step in χ_e coming from the increase in T_e (which would be visible for 1 ms time resolution as in the experiment, shown in figure 4.21) is very large, which justifies a large step in the experimental data. Similarly to the electron temperature and its gradient, the change occurs later and becomes smoother for larger radii.
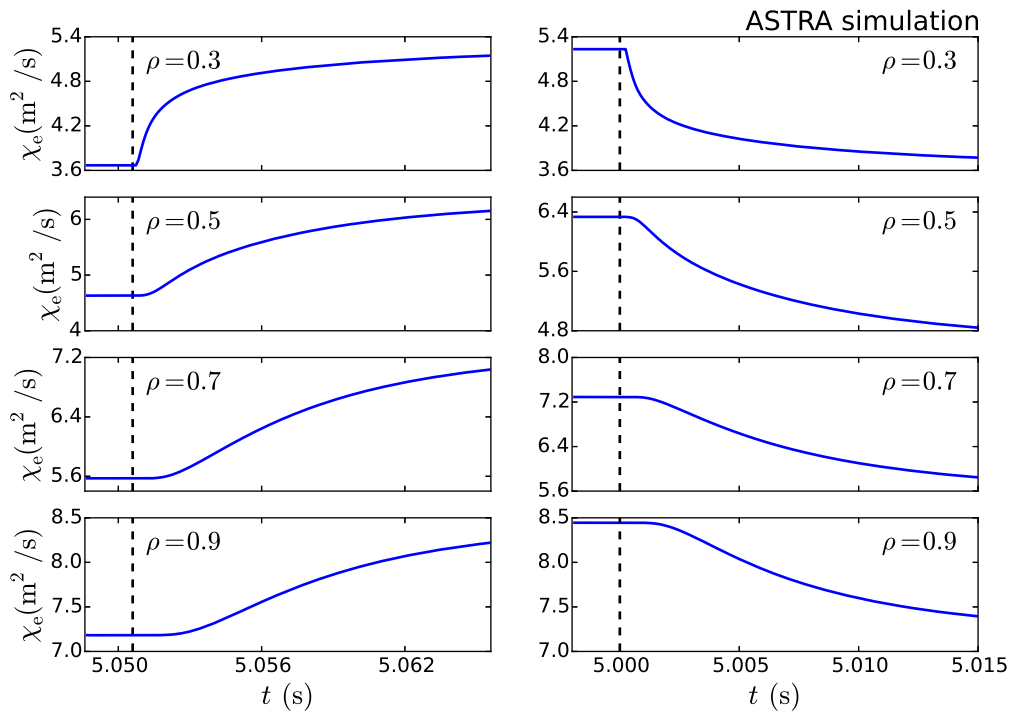
Figure 5.4: Temporal evolution of the simulated electron transport coefficient after stepwise increasing (left) and decreasing (right) ECRH power.

Chapter 6

Experimental Results from Wendelstein 7-X

This chapter reports on experiments done at the Wendelstein 7-X stellarator. The data shown in this chapter were measured in the first operational campaign OP 1.1.

6.1 General Remarks on W7-X Experiments

Power balance considerations for stellarator and tokamaks are slightly different, as for stellarators there is no Ohmic heating power, however, due to the lack of toroidal symmetry, measurements of global quantities (e.g. P_{rad}) are not always reliable. At the moment of writing this thesis the only heating system at W7-X is ECRH. The gas inside the torus just becomes a plasma when ECRH is switched on so solely discharges where power steps are performed on top of background heating power are considered. Another constraint is a constant density shortly before and after suddenly changing the heating power. Interferometers provide density measurements at good time resolution, however, density profiles are only available every 100 ms as this is the time resolution of the TS diagnostic. The radiated power is measured by several bolometer lines of sight. For non-local transport investigations, two plasma discharges (#20160303.007 and #20160309.026) conducted in March 2016 are examined. Figure 6.1 shows the ECRH power which is increased and decreased stepwise with a different (green) and the same (blue) magnitude on top of a background gyrotron, respectively.
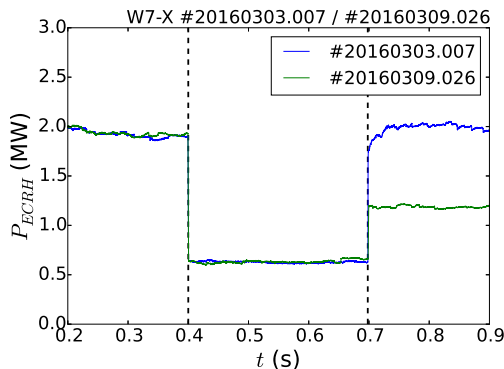
Figure 6.1: Different power steps of ECR heating in two W7-X plasma discharges.

6.2 Electron Temperature Evolution

At W7-X, ECE usually measures with a low field side antenna, but also provides data from beyond the magnetic axis (i.e. the high field side), which is more reliable and therefore solely used in the context of this thesis. Figure 6.2 depicts electron temperature profiles for the stationary states (dashed and full black line) and for the transient states (colours). In (a) the ECRH power (deposited in the plasma centre) is increased from 0.63 to 1.16 MW ($t = 0.4$ s), in (b) it is reduced from 0.63 to 1.16 MW ($t = 0.7$ s). Both, (a) and (b) start from the dashed line in stationary state whereas the lines in colours represent the temperature profiles in transient states. The time it takes the temperature at one radial location to rise (corresponding to τ in the fit function (equation 4.1) of the temperature response to heating changes at AUG) is larger than for ASDEX Upgrade: the profiles 50 ms after a heating step (green) are still farther away from the stationary state profiles (black full lines) than it is depicted in figure 4.3.

The same behaviour is plotted in figure 6.3, which shows the temperature evolution at different radii. Channels further away from the heating deposition react later to the change in ECRH power (dashed line). Due to high measurement noise, fits as done in section 4.2.2 do not converge on the small time window, simple by eye observations show that the time it takes the heat pulse to reach $\rho_{\text{tor}} = 0.7$ is a couple of ms which is higher than for ASDEX Upgrade where within this time the
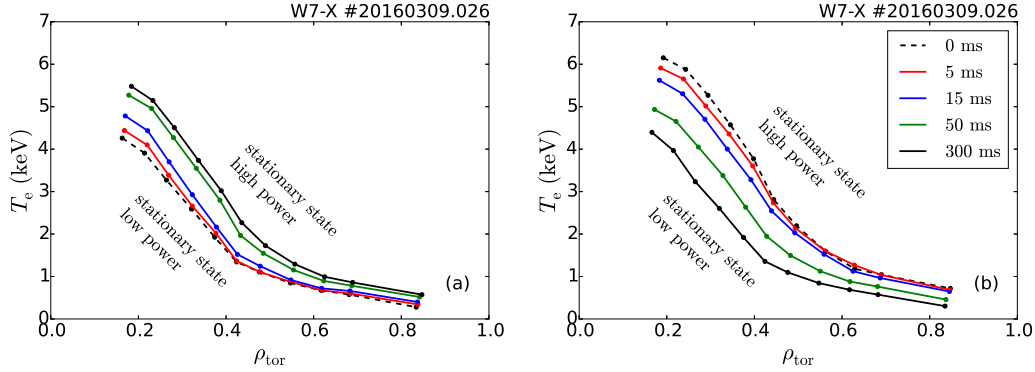
Figure 6.2: Temperature profile evolution for switching on 0.53 MW (a) and off 1.30 MW (b) ECRH power on top of a background ECRH power of ≈ 0.63 MW.

heat pulse has already reached the separatrix. Consequently the energy confinement time is found to be larger at W7-X than at ASDEX Upgrade.

6.3 Power Balance

Analogous to section 4.3.1 the kinetic energy of the electrons is calculated by numerical integration using equation 2.18. T_e is taken from the ECE diagnostic, n_e from the TS diagnostic. The volume inside a magnetic flux surface is calculated from ρ_{tor} and r_{eff}, respectively, by using the definition: $V = 2\pi^2 R r_{eff}^2$. As the ECE data only covers the radial region of $0.20 < \rho_{tor} < 0.83$, the electron temperature outside of this needs to be approximated by estimations. The electron energy contribution from the central region is negligible due to the small plasma volume, $T_e(0 < \rho_{tor} < 0.2) = T_e(\rho_{tor} = 0.2)$ is assumed. The edge region on the other hand contributes more than 10 % to the total energy. A reasonable assumption is $T_e(\rho_{tor} = 1) = 70$ keV and interpolating $T_e(0.83 < \rho_{tor} < 1)$ linearly between $T_e(\rho_{tor} = 0.83)$ and $T_e(\rho_{tor} = 1)$. Figure 6.4 (a) depicts the total electron energy over time. The sudden step at $t = 0.57$ s is related to a large change in density between two time points (time resolution is 100 ms). The red points in figure 6.4 (a) correspond to electron energies calculated the same way but using electron temperature data measured by TS. In the following both energies shall be abbreviated by $W_{e,ECE}$ and $W_{e,TS}$, respectively. The discrepancy between these two and an en-
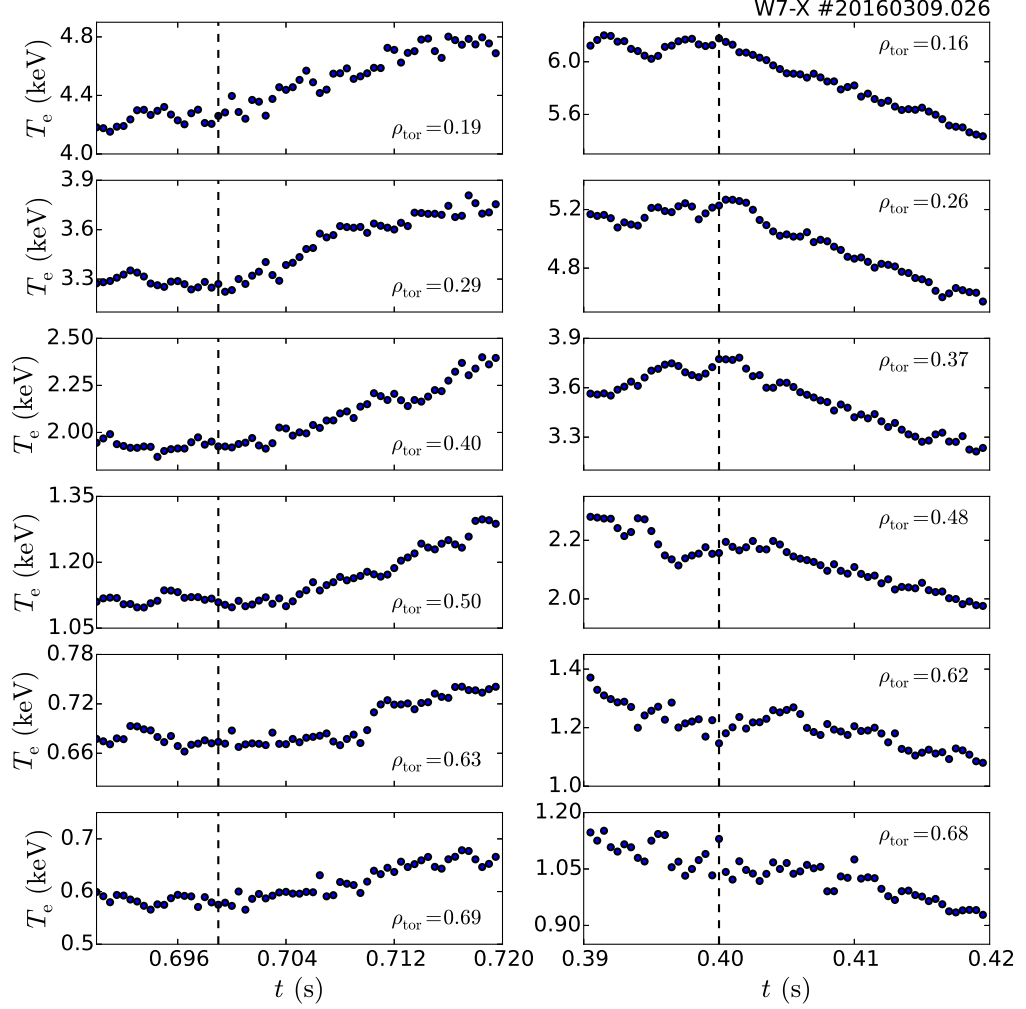
Figure 6.3: Temporal evolution of the electron temperature measured by ECE at different magnetic flux surfaces while adding (left) and removing (right) ECRH power.

ergy from a third source, the so-called *diamagnetic loop* which measures the plasma energy via induction, is an issue of ongoing research [33]. In addition, the choice of $T_e(0.83 < \rho_{tor} < 1)$ has a very large impact on $W_{e,ECE}$. Uncertainties are also included calculating the integral via the Riemann sum. However, as $W_{e,ECE}$ is al-
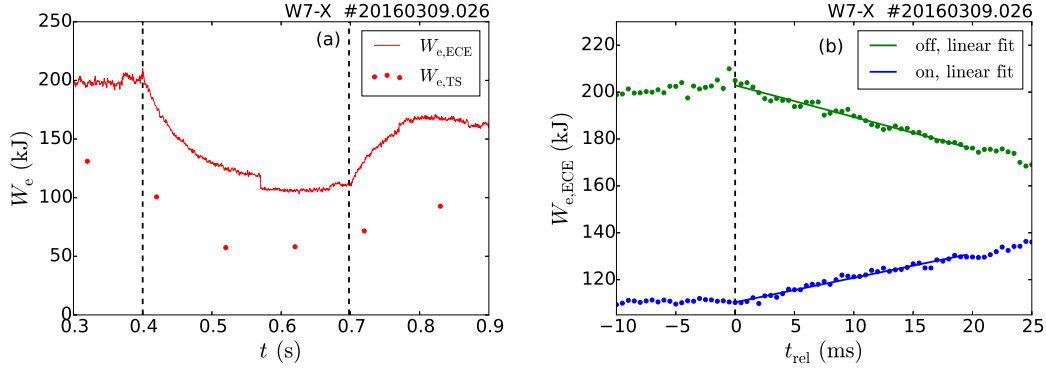
Figure 6.4: Total electron plasma energy W_{e} (a) and its response to power steps (black dashed lines) in ECRH (b).

ways larger than $W_{\mathrm{e,TS}}$, the power balance equation will not be considered using only $W_{\mathrm{e,ECE}}$, but also using $W_{\mathrm{e,ECE}}$ normalised on the data points of $W_{\mathrm{e,TS}}$. The latter one should give an estimate of the behaviour of $W_{\mathrm{e,TS}}$ if it had larger time resolution and shall be referred to the "normalised $W_{\mathrm{e,ECE}}$" or $W_{\mathrm{e,ECE \to TS}}$. A zoom into the response of the total electron energy (points) on heating is shown in figure 6.4 (b). The green colour corresponds to the power step at $t = 0.4$ s where ECRH is decreased, the blue colour represents the power step at $t = 0.7$ s where an additional gyrotron is added. For W7-X energies a linear function (full line) suits better to fit the first few milliseconds after the power step than the exponential function used for AUG. This could be another sign of higher energy confinement time in W7-X, as the linear rise time of the electron energy gives the time the heat pulse travels to the edge. The density within one fit interval is constant, which is to a large degree fulfilled according to line integrated interferometer data.

Figure 6.5 shows all terms considered for the electron power balance equation at W7-X for $\rho_{\mathrm{tor}} = 1$ (c.f. equation 2.17). Following the argumentation at ASDEX Upgrade given in section 4.3.3, the ion energy is assumed to be constant due to negligible electron-ion coupling. The change of the radiated power (red) after the ECRH power (green) step is small. The time derivative of the electron energy (blue) is obtained from the slope of linear fits on sliding time intervals of 20 ms with 50 % overlap. Assuming P_{rad} to be constant, the time derivative of the electron energy must equal ΔP_{ECRH} infinitesimally after t_{heat}. The dotted green line is the ECRH power shifted
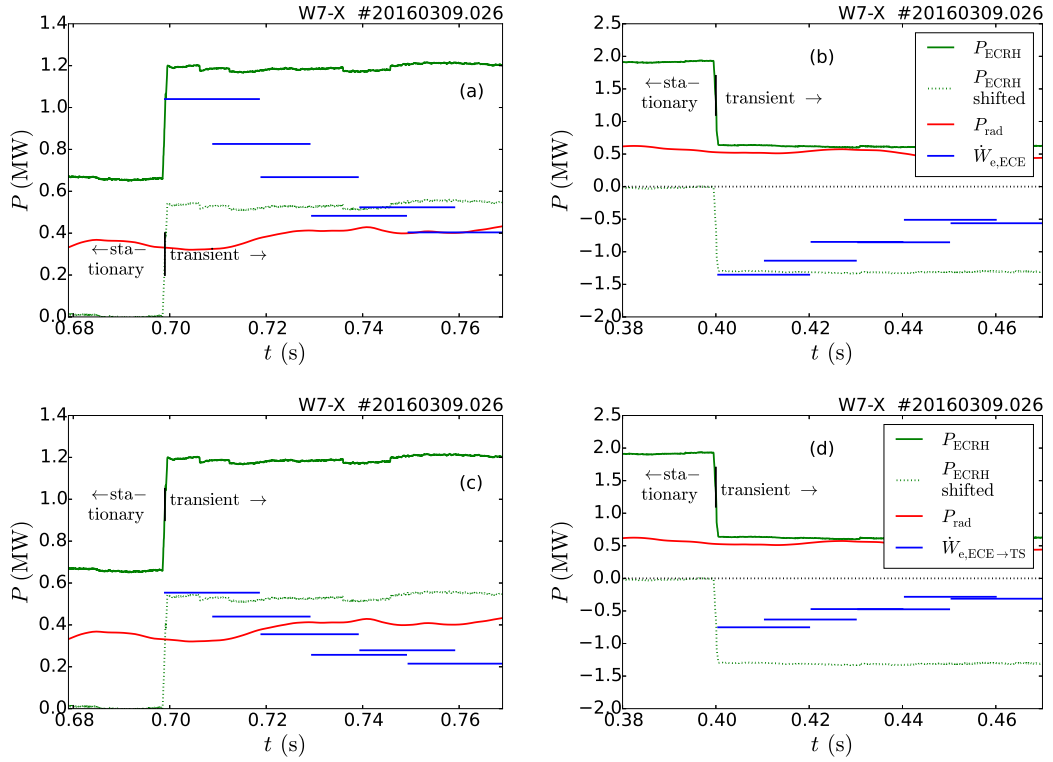
Figure 6.5: Total electron power balance with the heating power, radiated power and time derivative of the electron energy, using $\dot{W}_{e,ECE}$ for (a),(b) and $\dot{W}_{e,ECE \to TS}$ for (c),(d).

by the background ECRH power and enables a fast comparison between ΔP_{ECRH} and $\dot{W}_e(t_{heat})$. Figures 6.5 (a),(b) show the power balance for the two switching times in #20160309.026 using $\dot{W}_{e,ECE}$ and (c),(d) using $\dot{W}_{e,ECE \to TS}$. In (b) and (c) the power step and the time derivative of the electron energy match, which points to local transport. However, the reliability of the data is not sufficient to draw firm conclusions, as becomes visible when comparing each (d) and (a) to (b),(c). (a) indicates a larger energy rise than expected from the heating power step, which in principle might be possible to explain[1], but which most probable is related to measurement uncertainties . In (d) the change in energy is smaller than the power

---

[1] This could occur in the transition of the low-confinement mode to the high-confinement mode: there the power flowing over the separatrix reduces over a short time scale due to suppressed transport in the edge, enabling $\dot{W}_e(t_{heat}) > \Delta P_{ECRH}$.

step, which means non-locality in transport, as the heat flux over the separatrix changes immediately whereas the electron temperature does not (c.f. figure 6.3).

According to figure 6.5 time it takes W_e after a power step to reach $1/e$ of its original value is $\tau_{\text{W7-X}} \approx 60$ ms, whereas figure 4.10 (c) indicates $\tau_{\text{AUG}} \approx 15$ ms for the experiments done on ASDEX Upgrade. This is another indication for a better energy confinement time at W7-X than at AUG.

Coming back to the search for non-local effects in the electron energy response on changes in ECRH, the following table lists the magnitude of the power steps of the two considered discharges. The slopes of the linear fits directly after the power steps of both, $W_{e,\text{ECE}}$ and $W_{e,\text{ECE}\rightarrow\text{TS}}$, together with the ratio between power step and corresponding slope are given.

	$\Delta P_{\textbf{ECRH}}$	$\dot{W}_{\textbf{e,ECE}}$	$\Delta P/\dot{W}_{\textbf{e,ECE}}$	$\dot{W}_{\textbf{e,ECE}\rightarrow\textbf{TS}}$	$\Delta P/\dot{W}_{\textbf{e,ECE}\rightarrow\textbf{TS}}$
(a)	-1.30 MW	-1.35 MW	0.96	-0.77 MW	1.68
(b)	0.53 MW	1.04 MW	0.51	0.57 MW	0.92
(c)	-1.26 MW	-1.10 MW	1.14	-0.99 MW	1.27
(d)	1.15 MW	1.38 MW	0.84	1.14 MW	1.01

Non-locality is indicated by ratios greater than one, local transport by ratios equal to one. Ratios smaller than one are assumed to be due to measurement uncertainties. According to [33] the equilibrium mapping i.e. the difference between the actual magnetic field configuration and the assumed configuration in vacuum brings in an error of 5 % and the diagnostics (TS) of 10 % and the uncertainties in Z_{eff} another 5 %. This means that the actual plasma energy might be only 80 % of $W_{e,\text{TS}}$, which would shift the data towards non-locality. However, due to the large uncertainties no significant statement can be given for W7-X data considered here.

Chapter 7

Summary and Outlook

7.1 Summary

Signatures of non-local heat transport have been searched for in the context of this thesis as they have been claimed to be found in other fusion research facilities like W7-AS, LHD and DIII-D. Focus was put on outwards electron heat transport in the transient state which was generated by stepwise changing the electron heating (ECRH) while keeping all other experimental parameters constant.

The research topic can be summarised in one question: does the power flux through one magnetic flux surface depend on local parameters only, or can transient states be found in experiment, which local transport models fail to describe?

Rephrasing this sentence reveals more questions: does the electron transport coefficient directly depend on the heating power, as for instance: will the electron transport coefficient far from a region where the heating power is suddenly changed (e.g. $\chi_e(\rho = 1)$) change stepwise because the heat flux over the separatrix suddenly changes after a power step, or is there a finite time it takes the heat pulse to propagate outwards which lets the edge transport coefficient react continuously? Does the temporal change of the plasma energy within a magnetic flux surface reflect the step in heating power inside of it or can one observe a missing power inducing non-local transport behaviour.

These questions have been in detail analysed in experiments done at the ASDEX Upgrade tokamak and the Wendelstein 7-X stellarator, as well as in simulations performed with the transport code ASTRA.

The spatially resolved power flux was calculated from the power balance equation and together with the temperature gradient and other local quantities was used to

determine the electron transport coefficient. Within the measurement uncertainties no indication of a stepwise increase of the latter one at radii far from the heating deposition was observed on AUG, however one limiting factor was the accuracy of the time derivative of the electron plasma energy which inhibited a significant statement. Local transport requires an unambiguous dependence of the heat flux on local quantities which has been validated for T_e, ∇T_e and n_e in the context of this thesis. An examination of hysteresis behaviour in transient state was carried out which is not limited to a short time window and is therefore more robust. Within the measurement uncertainties no hysteresis behaviour and thus no indication for non-locality in the electron heat transport could be found.

Simulations assuming local transport, performed with the ASTRA code for the ASDEX Upgrade experiments show a consistent evolution of several simulated plasma parameters such as the electron temperature, its gradient and the density with the experimental data. It was demonstrated that hystereses in graphs plotting q_e/n_e over ∇T_e also arise for the local transport models which include gyro-Bohm scaling. From the predicted dependence of χ_e and thus q_e on $T_e^{3/2}$, it was concluded that they do not necessarily point to non-locality in transport, as it was assumed in previous works [19],[20].

Analyses done at W7-X investigated if the power balance equation of the whole plasma was fulfilled during the transient state. They were imposed to large uncertainties allowing non-local effects in transport neither to be excluded nor to be confirmed.

In conclusion, based on careful experiments and the accompanying simulations, non-local transport cannot be reported to be observed.

7.2 Outlook

The performed experiments cover the major points to examine non-local transport behaviour. As no clear indication of non-local effects have been found, only a very short outlook shall be given here. Further emphasis could be put on the first few milliseconds after a power step on ASDEX Upgrade plasmas, whereas the next step for W7-X would be a more detailed study about possible non-local effects to obtain significant results.

Bibliography

[1]   *United Nations - World Population Prospects 2017*. [Online; 23. Aug. 2017].
      URL: https://esa.un.org/unpd/wpp/DataQuery/.

[2]   *Annual Report 2016, Embracing Tipping Points*. Tech. rep. European Climate
      Foundation, 2016.

[3]   *Renewable Energies in Europe 2017, Recent growth and knock-on effects*. Tech.
      rep. European Environment Agency, 2017.

[4]   International Fusion Research Council (IFRC). 'Status report on fusion re-
      search'. In: *Nucl. Fusion* 45 (2005), A1.

[5]   *Climate CoLab - Teaching Fusion To The Public*. [Online; 10. Oct.
      2017]. URL: https : / / climatecolab . org/ contests/ 2015/ energy -
      supply/c/proposal/1314407.

[6]   J. Wesson. *Tokamaks. (The Oxford engineering science series; 20)*. Volume 1.
      OXFORD SCIENCE PUBLICATIONS, 1987.

[7]   T. S. Pedersen et al. 'Confirmation of the topology of the Wendelstein 7-X
      magnetic field to better than 1:100,000'. In: *Nat. Commun.* 7 (2016), p. 13493.

[8]   U. Stroth. *Plasmaphysik*. Volume 1. Vieweg + Teubner Verlag, 2011.

[9]   F. Ryter et al. 'Experimental studies of electron transport'. In: *Plasma Phys.
      Control. Fusion* 43 (2001), A323.

[10] F. Ryter et al. 'Experimental evidence for the key role of the ion heat channel
      in the physics of the L–H transition'. In: *Nucl. Fusion* 54 (2014), p. 083003.

[11] X. Garbet et al. 'Profile stiffness and global confinement'. In: *Plasma Phys.
      Control. Fusion* 46 (2004), p. 1351.

[12] H. Nordman et al. 'Simulation of toroidal drift mode turbulence driven by tem-
      perature gradients and electron trapping'. In: *Nucl. Fusion* 30 (1990), p. 983.

[13] A. G. Peeters et al. 'Linear gyrokinetic stability calculations of electron heat dominated plasmas in ASDEX Upgrade'. In: *Phys. Plasmas* 12 (2005), p. 022505.

[14] K. Ida et al. 'Towards an emerging understanding of non-locality phenomena and non-local transport'. In: *Nucl. Fusion* 55 (2015), p. 013022.

[15] *ASTRA Manual, Automated System for TRansport Analysis*. Tech. rep. Max-Planck Institute for Plasma Physics, 2002.

[16] U. Stroth et al. 'Fast transport changes and power degradation in the W7-AS stellarator'. In: *Plasma Phys. Control. Fusion* 38 (1996), p. 611.

[17] FOM ECRH Team et al TFR Group. 'The electron cyclotron resonance experiment on TFR'. In: *Nucl. Fusion* 28 (1988), p. 1995.

[18] K. W. Gentle et al. 'Electron energy transport inferences from modulated electron cyclotron heating in DIII-D'. In: *Phys. Plasmas* 13 (2006), p. 012311.

[19] K. Itoh et al. 'Hysteresis and Fast Timescale in Transport Relation of Toroidal Plasmas'. In: *Nucl. Fusion* 57 (2016), p. 102021.

[20] S. Inagaki et al. 'How is turbulence intensity determined by macroscopic variables in a toroidal plasma'. In: *Nucl. Fusion* 53 (2013), p. 113006.

[21] *Max Planck Institut für Plasmaphysik - ASDEX Upgrade Introduction*. [Online; 08. Sep. 2017]. URL: http://www.ipp.mpg.de/10268/einfuehrung.

[22] F. Ryter et al. 'Experimental Characterization of the Electron Heat Transport in Low-Density ASDEX Upgrade Plasmas'. In: *Phys. Rev. Lett.* 86 (2001), p. 5498.

[23] H. Murmann et al. 'The Thomson scattering systems of the ASDEX upgrade tokamak'. In: *Rev. Sci. Instrum.* 63 (1992), p. 4941.

[24] M. Willensdorfer et al. 'Characterization of the Li-BES at ASDEX Upgrade'. In: *Plasma Phys. Control. Fusion* 56 (2014), p. 025008.

[25] R Fischer et al. 'Integrated data analysis of profile diagnostics at ASDEX Upgrade'. In: *Fusion Sci. Technol.* 58 (2010), p. 675.

[26] R. J. Fonck. 'Charge exchange recombination spectroscopy as a plasma diagnostic tool'. In: *Rev. Sci. Instrum.* 56 (1985), p. 885.

[27] E. Viezzer et al. 'High-resolution charge exchange measurements at ASDEX Upgrade'. In: *Rev. Sci. Instrum.* 83 (2012), p. 103501.

[28] *Max Planck Institut für Plasmaphysik - Wendelstein 7-X.* [Online; 11. Oct. 2017]. URL: `http://www.ipp.mpg.de/16931/einfuehrung`.

[29] *The CLISTE Interpretative Equilibrium Code.* Tech. rep. Max-Planck Institute for Plasma Physics, European Atomic Energy Community, 1999.

[30] E. Poli et al. 'TORBEAM, a beam tracing code for electron-cyclotron waves in tokamak plasmas'. In: *Computer Physics Communications* 136 (2001), p. 90.

[31] R. J. Hawryluk et al. 'An empirical approach to tokamak transport'. In: *Physics of plasmas close to thermonuclear conditions* 1 (1980), p. 19.

[32] M. Bernert. 'Analysis of the H-mode density limit in the ASDEX Upgrade tokamak using bolometry'. PhD thesis. LMU Munich, 2013.

[33] G. Fuchert et al. 'Global energy confinement in the initial limiter configuration of Wendelstein 7-X'. In: *Nucl. Fusion* (paper in preparation).

Affirmation

I hereby certify that for this thesis I have worked independently and used no other than the specified sources, references and resources.

Garching, the

Klara Höfler

Danksagung

Ich möchte mich an dieser Stelle bei allen sehr herzlich bedanken, die mir während meiner Masterarbeit, in der Forschungsphase und beim Schreiben geholfen haben!

Mein besonderer Dank gilt Tim Happel, der sich jederzeit selbstverständlich und sehr geduldig mit meinen Fragen und Problemen beschäftigte, ob physikalisch, technisch, bei der Experimentplanung, in der wissenschaftlichen Formulierung oder im alltäglichen Institutsleben. Herzlich danken möchte ich auch François Ryter für seine Unterstützung bei ASTRA, seine laufenden Inputs zu Physik und Experimenten und den Kommentaren zur geschriebenen Arbeit. Bedanken möchte ich mich auch bei Pascale Hennequin, die trotz der örtlichen Distanz ihres Arbeitsplatzes zu Garching einen Teil meiner Betreuung übernahm und sehr hilfreiches Feedback gab.

Vielen Dank an Ulrich Stroth für die Initiierung meiner Masterarbeit, regelmäßige Diskussionen meiner Fortschritte und weiterer Vorgehensweise, dafür, mir je zwei Reisen nach Greifswald und zu den DPG Frühjahrstagungen ermöglicht zu haben und für sein Nachsehen, manche Falschnachrichten, nicht-lokalen Transport doch entdeckt zu haben, geduldig hingenommen zu haben. Ausdrücklich danken möchte ich auch Gregor Birkenmaier für einige physikalische Diskussionen und im Besonderen für seine Unterstützung bei der Entscheidung, mich in Richtung Fusionsforschung orientieren zu wollen.

Hervorheben möchte ich auch die große Hilfsbereitschaft, die mir aus Greifswald von Udo Höfel, Matthias Hirsch und Golo Fuchert entgegengebracht wurde, sowohl die herzliche Betreuung vor Ort, als auch per E-Mail und Telefon.

Dank gilt auch meinen Bürokollegen Thomas Reichbauer, Johannes Illerhaus und Alexander Bauer für die lustige gemeinsame Zeit, deren Hilfe bei diversen Prob-